



Contents lists available at ScienceDirect

Remote Sensing of Environment

journal homepage: www.elsevier.com/locate/rse

Bayesian methodology for inverting satellite ocean-color data

Robert Frouin ^{a,*}, Bruno Pelletier ^b^a Scripps Institution of Oceanography, University of California, San Diego, 9500 Gilman Drive, La Jolla, CA 92093-0224, USA^b IRMAR, Department of Mathematics, Université Rennes 2, CNRS, UEB, Place du Recteur Henri Le Moal, 35043 Rennes Cedex, France

ARTICLE INFO

Article history:

Received 8 June 2013

Received in revised form 29 November 2014

Accepted 5 December 2014

Available online xxxx

Keywords:

Remote sensing

Ocean color

Atmospheric correction

Inverse problem

Bayesian statistics

ABSTRACT

The inverse ocean color problem, i.e., the retrieval of marine reflectance from top-of-atmosphere (TOA) reflectance, is examined in a Bayesian context. The solution is expressed as a probability distribution that measures the likelihood of encountering specific values of the marine reflectance given the observed TOA reflectance. This conditional distribution, the posterior distribution, allows the construction of reliable multi-dimensional confidence domains of the retrieved marine reflectance. The expectation and covariance of the posterior distribution are computed, which gives for each pixel an estimate of the marine reflectance and a measure of its uncertainty. Situations for which forward model and observation are incompatible are also identified. Prior distributions of the forward model parameters that are suitable for use at the global scale, as well as a noise model, are determined. Partition-based models are defined and implemented for SeaWiFS, to approximate numerically the expectation and covariance. The ill-posed nature of the inverse problem is illustrated, indicating that a large set of ocean and atmospheric states, or pre-images, may correspond to very close values of the satellite signal. Theoretical performance is good globally, i.e., on average over all the geometric and geophysical situations considered, with negligible biases and standard deviation decreasing from 0.004 at 412 nm to 0.001 at 670 nm. Errors are smaller for geometries that avoid Sun glint and minimize air mass and aerosol influence, and for small aerosol optical thickness and maritime aerosols. The estimated uncertainty is consistent with the inversion error. The theoretical concepts and inverse models are applied to actual SeaWiFS imagery, and comparisons are made with estimates from the SeaDAS standard atmospheric correction algorithm and in situ measurements. The Bayesian and SeaDAS marine reflectance fields exhibit resemblance in patterns of variability, but the Bayesian imagery is less noisy and characterized by different spatial de-correlation scales. Experimental errors obtained from match-up data are similar to the theoretical errors determined from simulated data. Regionalization of the inverse models is a natural development to improve retrieval accuracy, for example by including explicit knowledge of the space and time variability of atmospheric variables.

© 2014 Elsevier Inc. All rights reserved.

1. Introduction

The classic approach to ocean-color remote sensing from space (Antoine & Morel, 1999; Gordon, 1997; Wang, 2010) consists of (i) estimating the aerosol reflectance in the red and near infrared where the ocean can be considered black (i.e., totally absorbing), and (ii) extrapolating the estimated aerosol reflectance to shorter wavelengths. The water reflectance is then retrieved by subtraction. This process is referred to as atmospheric correction. Depending on the application context, the retrieved water reflectance may then be related to chlorophyll-a concentration using a bio-optical model, semi-analytical or empirical (e.g., O'Reilly et al., 1998), or used in inverse schemes of varied complexity to estimate optical properties of suspended particles and dissolved organic matter (see Lee, 2006).

The process of atmospheric correction is inherently difficult to achieve with sufficient accuracy, since only a small fraction (10% or less) of the measured signal may originate from the water body. Furthermore, the surface and atmospheric constituents, especially aerosols, whose optical properties are influential, exhibit high space and time variability. However this two-step approach has been successful, and it is employed in the operational processing of imagery from most satellite ocean-color sensors. Variants and improvements to the classic atmospheric correction scheme have been made over the years, especially to deal with non-null reflectance in the red and near infrared, a general situation in estuaries and the coastal zone. The improvements in these regions consider spatial homogeneity for the spectral ratio of the aerosol and water reflectance in the red and near infrared (Ruddick, Ovidio, & Rijkeboer, 2000) or for the aerosol type, defined in a nearby non-turbid area (Hu, Carder, & Muller-Karger, 2000). They also use iteratively a bio-optical model (Bailey, Franz, & Werdell, 2010; Siegel, Wang, Maritorena, & Robinson, 2000; Stumpf, Arnone, Gould, Martinolich, & Ransibrahmanakul, 2003), exploit differences in the spectral shape of the aerosol and marine reflectance (Lavender, Pinkerton, Moore, Aiken,

* Corresponding author.

E-mail addresses: rfrouin@ucsd.edu (R. Frouin), bruno.pelletier@univ-rennes2.fr (B. Pelletier).

and Blondeau-Patissier (2005), or make use of observations in the short-wave infrared, where the ocean is black, even in the most turbid situations (Bo-Cai, M.M.J.A.Z., & D.C.O., 2000; Oo et al., 2008; Wang, Son, & Shi, 2009; Wang, Tang, & Shi, 2007).

Other empirical approaches to atmospheric correction have been proposed in the literature. In Frouin, Deschamps, Gross-Colzy, Murakami, and Nakajima (2006), the TOA reflectance in selected spectral bands is combined linearly, so that the atmosphere/surface effects are reduced substantially or practically eliminated. This algorithm assumes that the perturbing signal, smooth spectrally, can be modeled by a low-order polynomial, and the polynomial is selected so that the linear combination is sufficiently sensitive to chlorophyll-a concentration. In Steinmetz, Deschamps, and Ramon (2011), the atmospheric reflectance is approximated by a polynomial with non-spectral and spectral terms that represent atmospheric scattering and surface reflection, including adjacency effects from clouds and white surfaces. The water reflectance is modeled as a function of chlorophyll concentration and a backscattering coefficient for non-algal particles, and spectral matching is applied to tune the atmospheric and oceanic parameters.

Another approach to satellite ocean-color inversion is to determine simultaneously the key properties of aerosols and water constituents by minimizing an error criterion between the measured reflectance and the output of a radiative transfer model (e.g., Chomko & Gordon, 1988; Kuchinke, Gordon, Harding, & Voss, 2009; Land & Haigh, 1996; Stamnes et al., 2007). This belongs to the family of deterministic solutions to inverse problems; for a mathematical treatment of the subject, we refer the interested reader to Engl, Hanke, and Neubauer (1996). Through systematic variation of candidate aerosol models, aerosol optical thickness, hydrosol backscattering coefficient, yellow substance absorption, and chlorophyll-a concentration, or a subset of those parameters, a best fit to the spectral top-of-atmosphere reflectance (visible and near infrared) is obtained in an iterative manner. The advantage of this approach, compared with the standard, two-step approach, resides in its ability to handle both Case 1 and Case 2 waters. It also can handle both weakly and strongly absorbing aerosols, even if the vertical distribution of aerosols, an important variable in the presence of absorbing aerosols, is not varied in the optimization procedure. A main drawback is that convergence of the minimizing sequence may be slow in some cases, making it difficult to process large amounts of satellite data. To cope with this issue, a variant proposed in Brajard, Jamet, Moulin, and Thiria (2006) and Jamet, Thiria, Moulin, and Crépon (2005) consists of approximating the operator associated to the radiative transfer (RT) model by a function which is faster in execution than the RT code, e.g., by neural networks. Still, convergence speed of the minimization algorithm remains an issue. It may also not be easy to differentiate absorption by aerosols and water constituents like yellow substances, processes that tend to decrease the TOA signal in a similar way. As a result, the retrievals may not be robust to small perturbations on the TOA reflectance. This reflects the fact that atmospheric correction is an ill-posed inverse problem; in particular, different values of the atmospheric and oceanic parameter can correspond to close values of the TOA reflectance. In the context of deterministic inverse problem, stability of the solution can be obtained by regularization (see Engl et al., 1996), but to the best of our knowledge, regularization strategies are not implemented in the approaches described above.

Another route is to cast atmospheric correction as a statistical inverse problem and to define a solution in a Bayesian context. In this setting, one group of approaches consists of estimating, based on simulations, a function performing a mapping from the TOA reflectance to the marine reflectance. In Shroeder, Behnert, Schaale, Fischer, and Doerffer (2007), a neural network model is fitted to simulated data. A similar approach is studied in Gross, Colzy, Frouin, and Henry (2007a,b), where the (finite-dimensional) TOA signal, corrected for gaseous absorption and molecular scattering, is first represented in a basis such that the correlation between the ocean contribution and atmosphere contribution is, to some extent, minimized. This representation of the TOA reflectance makes

the function approximation problem potentially easier to solve. In these studies, data are simulated for all the observation geometries. In Frouin and Pelletier (2007) and Pelletier and Frouin (2004, 2005), the angular information is decoupled from the spectral reflectance, and atmospheric correction is considered as a collection of similar inverse problems indexed by the observation geometry. These methods can all be formalized in a Bayesian context; see Kaipio and Somersalo (2004) and Tarantola (2005) for an introduction on the subject.

The Bayesian approach to inverse problem consists of first specifying a probability distribution, called the prior distribution, on the input parameters (atmospheric and oceanic) of the RT model. As the name implies, the prior distribution reflects prior knowledge that may be available before the measurement of the TOA reflectance. A probabilistic modeling of any perturbation of the TOA reflectance is also typically considered, in the form of an additive random noise. The solution to the inverse problem is then expressed as a probability distribution which, in the present context of atmospheric correction, measures the likelihood of encountering values of water reflectance given the TOA reflectance (i.e., after it has been observed). The posterior distribution is a very rich object, and its complete reconstruction and exploration can rapidly become prohibitive from the computational side. Instead, one may reduce the ambition to extracting useful quantities, like its expectation and covariance. In the present setting of atmospheric correction, the expectation provides an estimate of the water reflectance, while the covariance allows a quantification of uncertainty in the water reflectance estimate.

In this paper, we address ocean-color remote sensing in a Bayesian context. We make the following contributions. First of all, we formulate the atmospheric correction problem at a certain depth of physical modeling, and we use the angular decoupling as in Frouin and Pelletier (2007) and Pelletier and Frouin (2004, 2005). Prior distributions suitable for use at a global scale, as well as a noise model, are determined. Second, we define and implement numerical approximations of the expectation and covariance of the posterior distribution (i.e., the complete Bayesian solution). The procedure is developed for the marine reflectance as well as for the atmospheric parameters, hence these quantities are retrieved simultaneously from the TOA reflectance, and measures of uncertainties are provided along with the retrievals. The modeling choices in this work have been governed by keeping the execution time of the models small, and by having theoretical guarantees on the performance. Let us point out that it is a forward model which is inverted and that, as precise as the physical modeling can be, it is important to detect cases where the model is limited in view of the measured TOA reflectance. So as a final contribution, we define and implement a model, based on level sets, to detect these situations where the retrievals become meaningless.

The paper is organized as follows. In Section 2, the inverse problem of atmospheric correction is defined, and the Bayesian solution is formulated. In Section 3, the inverse applications that will be implemented in practice are specified. In Sections 4 and 5, the modeling of the satellite signal and the approximation of the forward operator are described. In Section 6, the practical implementation of the inverse applications is detailed. Some technical details are gathered in Appendices A and B at the end of the paper. In Section 7, performance is evaluated on simulated data, and the ill posed-ness of the inverse problem is illustrated and discussed. In Section 8, the theoretical concepts and inverse models are applied to Sea-viewing Wide Field-of view Sensor (SeaWiFS) imagery, and comparisons are made with estimates from the standard atmospheric correction algorithm and in-situ measurements. In Section 9, conclusions are given about the Bayesian methodology in terms of performance, robustness, and generalization, as well as a perspective on future work.

2. Bayesian approach to atmospheric correction

2.1. Problem position

Let L_{toa} be the radiance measured by the satellite ocean-color sensor in a given spectral band. Express L_{toa} in terms of bidirectional reflectance

ρ_{toa} as $\rho_{toa} = \pi L_{toa} / (F_s \cos(\theta_s))$, where F_s is the extraterrestrial solar irradiance (corrected for Earth-Sun distance), and where θ_s is the Sun zenith angle. In clear sky conditions (i.e., a cloudless atmosphere), following lines devised in Tanré, Herman, Deschamps, and De Leffe (1979), ρ_{toa} may be modeled as

$$\rho_{toa} = T_g \left[\rho_{mol} + \rho_{aer} + \rho_{mol-g} + \rho_{aer-g} + \rho_{mol-aer} + \rho_g t_a + \frac{T_a \rho_f}{1 - S_a \rho_f} + \frac{T_a \rho_w}{1 - S_a \rho_w} \right], \quad (1)$$

where T_g is the gaseous transmittance (accounts for absorption of photons by nitrous oxide, ozone, oxygen, and water vapor), ρ_{mol} and ρ_{aer} are the molecular and aerosol reflectance (account for multiple scattering of photons by molecules or aerosols only), ρ_{mol-g} and ρ_{aer-g} account for interactions between molecules or aerosols and photons reflected by a wavy surface, $\rho_{mol-aer}$ accounts for the coupling between scattering by molecules and scattering and absorption by aerosols, ρ_g is the Sun glint reflectance, t_a and T_a are the direct and total (direct plus diffuse) transmittance of the atmosphere along the path Sun-to-surface and surface-to-sensor, ρ_f accounts for backscattering of photons by white-caps, S_a is the spherical albedo of the atmosphere (accounts for successive photon interactions with the surface, the atmosphere, and the surface again), and ρ_w is the water reflectance (accounts for photons backscattered by the water body). In this decomposition, the perturbing signal from the atmosphere and surface is completely separated from the water body contribution. A more accurate modeling would be to replace the sum of the last two terms in Eq. (1) by $(\rho_f + \rho_w) / [1 - S_a(\rho_f + \rho_w)]$, but the decomposition is justified because ρ_f , ρ_w , and S_a are small compared with unity.

In the presence of molecules only, the top-of-atmosphere signal from the atmosphere and surface ($\rho_w = 0$) is reduced to:

$$\rho_{toa}^0 = T_g \left[\rho_{mol} + \rho_{mol-g} + \rho_g t_{mol} + \frac{T_{mol} \rho_f}{1 - S_{mol} \rho_f} \right], \quad (2)$$

where t_{mol} , T_{mol} , and S_{mol} are respectively the direct transmittance, the total transmittance, and the spherical albedo for molecules. Define the quantities ρ and ρ_a respectively by

$$\rho = \frac{1}{T_g} (\rho_{toa} - \rho_{toa}^0), \quad (3)$$

and

$$\rho_a = \rho_{aer} + \rho_{aer-g} + \rho_{mol-aer} + \rho_g t_a - \rho_g t_{mol} + \frac{T_a \rho_f}{1 - S_a \rho_f} - \frac{T_{mol} \rho_f}{1 - S_{mol} \rho_f}. \quad (4)$$

Then we have:

$$\rho = \rho_a + \frac{T_a \rho_w}{1 - S_a \rho_w}. \quad (5)$$

The inner term in the right-hand side of Eq. (2) can be accurately computed from atmospheric pressure and wind speed, while T_g can be well approximated in the spectral bands of ocean-color sensors given the absorber amounts along the optical path. Consequently, ρ_{toa}^0 can be evaluated at the same time as the measurement of ρ_{toa} , which can thus be converted to ρ using Eq. (3). Note that transforming ρ_{toa} to ρ by Eq. (3) amounts at first correcting ρ_{toa} for gaseous absorption and next at subtracting for known effects due to molecules only. This pre-processing enhances the relative contribution of the ocean signal into ρ and, importantly, diminishes the influence of air pressure and wind speed. Henceforth, the term "observed reflectance" will refer to this corrected reflectance unless otherwise noted.

In actuality, the observed reflectance departs from the range of the theoretical model (5) due to measurement errors and modeling uncertainties. To represent these sources of variability, we shall add a random noise term ε , leading to the statistical model

$$\rho = \rho_a + \frac{T_a \rho_w}{1 - S_a \rho_w} + \varepsilon. \quad (6)$$

All the variables in Eq. (6) are functions of the wavelength λ and depend on the observation geometry (i.e., relative position of the Sun and sensor with respect to the target). The observed data is finite-dimensional and is a vector $y = (y_1, \dots, y_d)$ of measurements of ρ in spectral bands centered at wavelengths $\lambda_1 < \dots < \lambda_d$, i.e., $y_i = \rho(\lambda_i)$, for $i = 1, \dots, d$.

With these notations, atmospheric correction refers to the process of estimating ρ_w from y and without knowledge of ρ_a , T_a and S_a in Eq. (5). Note that since only y is observed, atmospheric correction is only one part of the complete inverse problem of estimating both the atmospheric and oceanic parameters from ρ , i.e., (ρ_a, T_a, S_a) and ρ_w , even if in atmospheric correction, interest is only in ρ_w .

2.2. Ill-posed nature of the inverse problem

Atmospheric correction is an ill-posed inverse problem: even without noise, i.e., in model (5), different states of the atmosphere and of the ocean may correspond to very close values of the satellite signal. To see this using model (5), denote by \mathcal{X}_a and \mathcal{X}_w two sets containing values for the triple (ρ_a, T_a, S_a) and the water reflectance ρ_w , respectively. Pick a point (ρ_a^*, T_a^*, S_a^*) in \mathcal{X}_a and a point ρ_w^* in \mathcal{X}_w , leading to a reflectance ρ^* according to Eq. (5). Fix a threshold $\delta > 0$, which represents a noise level on ρ , and consider all the possible combinations of (ρ_a, T_a, S_a) and ρ_w such that $\rho_a + T_a / (1 - S_a \rho_f)$ is at a distance no more than δ from ρ^* . These combinations are the pre-images of a ball of radius δ by the operator mapping $((\rho_a, T_a, S_a), \rho_w)$ to ρ according to Eq. (5).

One example of pre-images is provided in Fig. 1. In this example, the reflectance ρ is evaluated in 8 spectral bands from the visible to the near infra-red, and the Euclidean distance on \mathbb{R}^8 is used. It is apparent in this case that quite different marine reflectance spectra are mapped to very close TOA reflectance spectra. As a consequence, in the presence of noise on the measurements, the uncertainty on the retrieved marine reflectance may be large. Naturally, the size of the set of pre-images depends on the choice of the threshold δ and on the search spaces \mathcal{X}_a and \mathcal{X}_w . The noise level on ρ is taken as $\delta = 0.001$, as will be justified further in the paper. The set \mathcal{X}_a results from considering realistic aerosol models in varied proportions and load, and the set \mathcal{X}_w is composed of in-situ water reflectance spectra corresponding mainly to Case I waters. Similar results (not displayed here) are obtained for other cases. Since the variability of the marine reflectance component of the pre-images can be rather large, as illustrated in Fig. 1, it is important to define and attach a measure of uncertainty to the retrieval of the marine reflectance from space.

2.3. Bayesian solution

Consider a finite-dimensional version of the statistical inverse problem (6) in which each quantity is evaluated at λ_i , for $i = 1, \dots, d$. To this end, let

$$x_{a,i} = (\rho_a(\lambda_i), T_a(\lambda_i), S_a(\lambda_i)) \text{ and } x_{w,i} = \rho_w(\lambda_i) \quad \text{for all } i = 1, \dots, d, \quad (7)$$

and let

$$x_a = (x_{a,1}, \dots, x_{a,d}) \in \mathcal{X}_a \subset \mathbb{R}^{3d} \text{ and } x_w = (x_{w,1}, \dots, x_{w,d}) \in \mathcal{X}_w \subset \mathbb{R}^d. \quad (8)$$

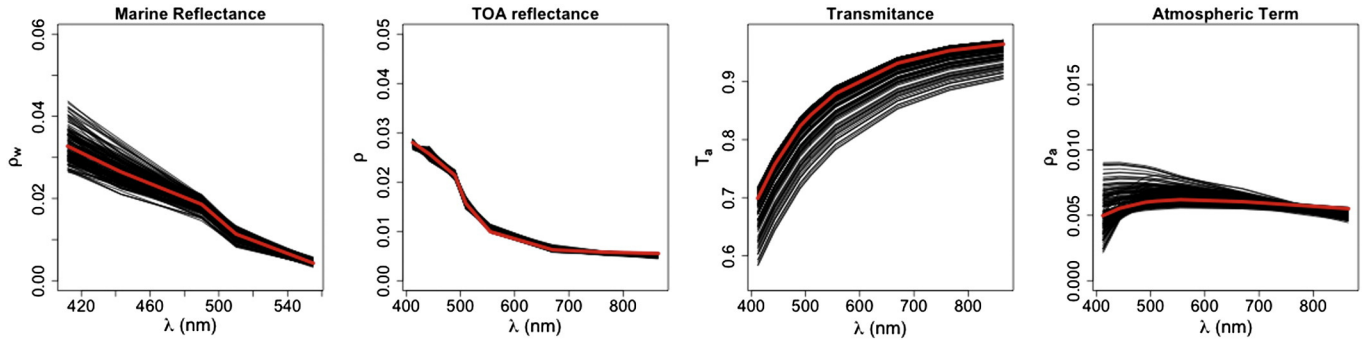


Fig. 1. Example of pre-images. Actual values of ρ_w , ρ , T_a and ρ_a are displayed in red, and the pre-images at a distance no more than δ (see text) are displayed in black.

The subsets \mathcal{X}_a and \mathcal{X}_w in the above equations are constraint sets for the atmospheric parameters and the marine reflectance components respectively. The model reads as

$$y = \Phi(x_a, x_w) + \varepsilon, \quad (9)$$

where ε is a random vector in \mathbb{R}^d , and where $\Phi: \mathcal{X}_a \times \mathcal{X}_w \rightarrow \mathbb{R}^d$ is the map with components $(\Phi_i)_{1 \leq i \leq d}$ defined by $\Phi_i(x_a, x_w) = \rho_a(\lambda_i) + T_a(\lambda_i)\rho_w(\lambda_i) / [1 - S_a(\lambda_i)\rho_w(\lambda_i)]$.

In the Bayesian approach, x_a , x_w , and y in Eq. (9) are treated as random variables. This defines a statistical model, and any vector of measurements y^{obs} is then considered as a realization of the random vector y in Eq. (9). To complete the definition of this model, there remains to specify a distribution \mathbb{P}_ε for the random noise ε , and a distribution for the pair (x_a, x_w) . The distribution of (x_a, x_w) is called the *prior distribution*. It describes, in a probabilistic manner, the prior knowledge one may have about x_a and x_w before the acquisition of the data y . Since there is no particular reason to expect that the atmospheric parameters and the marine reflectance should be correlated, such a distribution will be a product measure of the form $\mathbb{P}_{x_a} \otimes \mathbb{P}_{x_w}$, where \mathbb{P}_{x_a} and \mathbb{P}_{x_w} are probability measures on \mathbb{R}^{3d} and \mathbb{R}^d , respectively. The prior distribution allows one to incorporate known constraints in the model. For instance, that x_a and x_w must belong to the constraint sets \mathcal{X}_a and \mathcal{X}_w is specified in the model by considering prior distributions \mathbb{P}_{x_a} and \mathbb{P}_{x_w} with support in \mathcal{X}_a and \mathcal{X}_w . At last, the noise ε in model (9) will be considered as independent from (x_a, x_w) . Hence the prior distribution together with the noise distribution completely specifies the joint distribution of (x_a, x_w, y) .

The Bayesian solution to the inverse problem of retrieving (x_a, x_w) from y is defined as the conditional distribution of (x_a, x_w) given y . This distribution, further denoted by $\mathbb{P}_{(x_a, x_w)|y}$, is called the *posterior distribution*. Hence, given the observation y^{obs} , the solution is expressed as the probability measure $\mathbb{P}_{(x_a, x_w)|y=y^{obs}}$. Note that the posterior distribution can be seen as a function of y^{obs} . From the computational side, though, the complete reconstruction of the posterior distribution is out of reach in many problems, despite the intense development of sampling techniques like Markov Chain Monte Carlo (MCMC). As an alternative, one can generally restrict the objective to only estimating some relevant characteristics of the posterior distribution, like its mean, its modes (i.e., points of local maximum), or its covariance matrix.

In this work, we define and implement models to approximate the mean and covariance matrix of the posterior distribution as functions of the observation y^{obs} . These models provide an estimate of the marine reflectance and a measure of uncertainty. They are introduced generally in Section 3 and the practical implementation is exposed in Section 6.

3. Inversion scheme

The construction of the solution, i.e., the estimation of the mean and covariance matrix of the posterior distribution, requires specifying the prior distributions and the noise distributions. These distributions are

defined in Section 3.1. They are intended to be representative of conditions that may be encountered at a global scale. The class of models that will be implemented to approximate the mean and covariance of the posterior distribution are introduced in Section 3.2. A quantity called a *p-value* is also defined, which allows one to detect those situations for which the observation y^{obs} is highly unlikely to have originated from model (9), in which case this latter cannot be used reliably for inversion purposes. As in our previous work (Frouin & Pelletier, 2007; Pelletier & Frouin, 2004, 2005), angular decoupling is used; the procedure is defined in Section 3.3. The implementation details of the models are described in Section 6.

3.1. Modeling the prior and noise distributions

A prior distribution on the marine and atmospheric parameters describes, in terms of frequencies, the knowledge one may have about these parameters before the acquisition of the satellite data. For instance, if it is known in advance that, for the considered location and time, only marine spectra corresponding to open ocean waters will be encountered, then the prior distribution \mathbb{P}_{x_w} should reflect that. This can be achieved by requesting that its support \mathcal{X}_w be composed only of spectra of this type.

For the marine reflectance, we shall first define a compact set \mathcal{X}_w composed of realistic values of the marine reflectance encountered at a global scale. Next, in the absence of other information (e.g., relative proportion of water type), the prior distribution will be taken as the uniform measure on \mathcal{X}_w . Defining \mathcal{X}_w could be achieved by considering several models relating the marine reflectance with biological parameters, but we find it more appropriate to base our analysis on in-situ measurement of the marine reflectance. Indeed, modeling marine reflectance from measurements of inherent optical properties (e.g., Garver & Siegel, 1997; Gordon et al., 1988; Morel & Maritorena, 2002; Park & Ruddick, 2005) does not fully take into account the natural correlations between controlling variables. For a given phytoplankton assemblage/population, absorption and backscattering coefficients are related in a unique way that is not captured in empirical bio-optical formulas determined from amalgamating measurements collected in diverse oceanic regions. Our analysis is therefore based on the NOMAD dataset (Werdell & Bailey, 2005), and on data acquired at several AERONET-OC sites (Zibordi et al., 2010).

To define the prior distribution \mathbb{P}_{x_a} on the atmospheric parameters, x_a is expressed as a function Φ_a of other parameters γ_a , taking values in some set Γ_a . To keep the exposition simple at this point, we just mention that γ_a is composed of physical variables with known range (pressure, wind speed), and of variables related to modeling of aerosol optical properties. As for the marine reflectance, uniform distributions will be considered for all these quantities, except for the aerosol optical thickness, for which we shall make use of the study by Knobelspiesse et al. (2004) which shows that, over the oceans, this latter is approximately log-normally distributed. Details are provided in Section 6.2.

The noise term ε in Eq. (9) is intended to encapsulate all the sources of uncertainty leading to model (9). Hence its distribution \mathbb{P}_ε describes the frequencies of the magnitude by which the actual observations deviate from the physical forward modeling. Herein, we shall assume that ε is a Gaussian random vector on \mathbb{R}^d with $\mathbb{E}\varepsilon = 0$ and $\text{Cov}(\varepsilon) = \sigma^2 \text{Id}_{\mathbb{R}^d}$. Naturally these assumptions are restrictive, but since the actual ocean color sensors measure the spectrum in a limited number of spectral bands, more general models (see e.g. Bissantz, Hohage, & Munk, 2004) cannot be considered. Let us point out that the parameter σ , which governs the hypothesized global noise level, is akin to the regularization parameter in Tikhonov regularization scheme, and has to be properly selected. For this purpose, we consider a large number of TOA observations and we estimate σ by maximum likelihood.

3.2. Approximating the posterior mean and covariance, and the p-value

The prior distribution $\mathbb{P}_{x_a} \otimes \mathbb{P}_{x_w}$ and the noise distribution \mathbb{P}_ε are now fixed as defined above, and expectations are taken according to these distributions. Recall that the Bayesian solution to the inverse problem is defined as the probability measure $\mathbb{P}_{(x_a, x_w)|y=y^{\text{obs}}}$. In this work, we focus on estimating only two characteristics of the posterior distribution, namely its mean and its covariance. Note that they depend on y^{obs} and that they correspond to the conditional mean and covariance of the marine reflectance given the observation y^{obs} defined respectively by

$$r(y^{\text{obs}}) = \mathbb{E}[x_w|y = y^{\text{obs}}] \quad \text{and} \quad \Sigma(y^{\text{obs}}) = \text{Cov}(x_w|y = y^{\text{obs}}). \quad (10)$$

A very large variety of numerical procedures and models may be employed to approximate the applications r and Σ . To guide our choice, we considered the following objectives: (i) that the models be fast in execution, suitable for use on an operational basis, and (ii) that the theoretical applications r and Σ be approximated with a guaranteed accuracy and in a reasonable computer time. Based on these requirements, we define models based on a common partition of \mathbb{R}^d and which are either constant or linear above each element of the partition.

Formally, denote by A_1, \dots, A_M the elements, also called cells, of a partition of \mathbb{R}^d . For any subset A of \mathbb{R}^d , denote by $\mathbf{1}_A(\cdot)$ the characteristic function of A , i.e., for any y in \mathbb{R}^d , $\mathbf{1}_A(y) = 1$ if y is in A and 0 otherwise. We consider models which are linear over each cell (for r) and constant over each cell (for Σ), i.e., models of the form

$$\hat{r}(y^{\text{obs}}) = \sum_{m=1}^M (\alpha_m + B_m y^{\text{obs}}) \mathbf{1}_{A_m}(y^{\text{obs}}) \quad \text{and} \quad \hat{\Sigma}(y^{\text{obs}}) = \sum_{m=1}^M C_m \mathbf{1}_{A_m}(y^{\text{obs}}), \quad (11)$$

where $\alpha_m \in \mathbb{R}^d$ and $B_m \in \mathcal{M}_d(\mathbb{R})$ for all $m = 1, \dots, M$, and where $C_m \in \mathcal{M}_d(\mathbb{R})$ is a covariance matrix, for all $m = 1, \dots, M$. Note that in the sums in Eq. (11), only one term is non-zero. From a numerical stand point, to process an observation y^{obs} using either of the models in Eq. (11), the first task is to determine which of the A_m among the M cells contain y^{obs} . To reduce the computational time of this operation, we shall use a partition induced by a perfect binary tree of depth K . This is a partition of \mathbb{R}^d into $M = 2^K$ elements which is structured in such a way that determining cell membership requires only K evaluations of a simple rule (this is advantageous to an unstructured partition that could require 2^K tests to determine cell membership).

Suppose that the partition A_1, \dots, A_M is fixed. Using a quadratic criterion (i.e., L^2 risk) to define optimality, the optimal coefficients $\hat{\alpha}_m$, \hat{B}_m , and \hat{C}_m , for $m = 1, \dots, M$ are given by

$$\begin{aligned} (\hat{\alpha}_m, \hat{B}_m) &\in \operatorname{argmin}_{\alpha, B} \mathbb{E}\left\{ \|\alpha + By - r(y)\|^2 \mathbf{1}_{A_m}(y) \right\} \quad \text{and} \\ \hat{C}_m &\in \operatorname{argmin}_C \mathbb{E}\left\{ \|C - \sum(y)\|^2 \mathbf{1}_{A_m}(y) \right\}, \end{aligned} \quad (12)$$

for all $m = 1, \dots, M$. Simple calculations allow one to derive explicit expressions for the optimal coefficients which, in turn, can be approximated numerically to any arbitrary accuracy. This is possible since the joint distribution of (x_a, x_w, y) is known.

At this point, the only remaining free parameter of model (11) is the partition A_1, \dots, A_M . It can be shown that, under mild conditions, the L^2 risk of these models will tend to zero as the partition is being refined. Basically, to ensure convergence, the number of cells must go to infinity while the cells have to shrink at an appropriate rate; we refer the reader interested in these aspects to Lugosi and Nobel (1999), Nobel (1996) and Gyorfi, Kohler, Krzyzak, and Walk (2002, chapters 4 and 13). In the present work, the partition is grown from a perfect binary tree of depth $K = 17$, which yield a total of $2^K = 131,072$ cells. The technical details of the construction are provided further in the paper. The main point here is that this partition gives a discretization of the set of possible values for the observed reflectance (i.e., \mathbb{R}^d for y in Eq. (9)).

It is essential to keep in mind that the proposed methodology only offers an inversion of the physical models considered in Eq. (1) and leading to Eq. (6). Then given the observation y^{obs} , how much confidence can be placed in the retrievals, including in the proposed uncertainties? In other words, how likely is y^{obs} to have originated from model (9)? It is therefore critical to, at least, detect situations where there is reasonable evidence that the observation y^{obs} is incompatible with the model. For this purpose, we define a procedure based on level sets as follows.

Denote by f_y the density of y in model (9). For any $t \geq 0$, denote by $\mathcal{L}(t)$ the upper level set of f_y at level t defined by $\mathcal{L}(t) = \{y \in \mathbb{R}^d : f_y(y) \geq t\}$. Under mild regularity conditions, it can be shown that the level sets of f_y are the sets having minimum volume among sets with a given probability content; see e.g., Polonik (1995, 1997). Given the observation y^{obs} , let $t(y^{\text{obs}})$ be the largest real number $t > 0$ such that y^{obs} belongs to $\mathcal{L}(t)$, i.e., $t(y^{\text{obs}}) = \sup\{t > 0 : y^{\text{obs}} \in \mathcal{L}(t)\}$. Then, we define the map p_V from \mathbb{R}^d to $(0; 1)$ by

$$p_V(y^{\text{obs}}) = \mathbb{P}(y \notin \mathcal{L}(t(y^{\text{obs}}))), \quad (13)$$

i.e., $p_V(y^{\text{obs}})$ is the probability that a new observation y does not belong to the level set $\mathcal{L}(t(y^{\text{obs}}))$. We shall refer to $p_V(y^{\text{obs}})$ as the p-value of y^{obs} . Therefore $p_V(y^{\text{obs}})$ can be interpreted as the probability that a new observation y be at least as extreme as the data y^{obs} . Hence a low value of $p_V(y^{\text{obs}})$, say lower than 1%, may indicate that the model and the observation are incompatible.

To construct an approximation of the p-value map p_V , we shall make use again of the partition A_1, \dots, A_M . For any $1 \leq m \leq M$, let $p_m = \mathbb{P}(y \in A_m)$ and define the density estimate

$$\hat{f}_y(y) = \sum_{m=1}^M \hat{f}_m \mathbf{1}_{A_m}(y) \quad \text{with} \quad \hat{f}_m = \frac{p_m}{\text{Vol}_d(A_m)}, \quad (14)$$

where it is implicitly assumed that $\text{Vol}_d(A_m) > 0$ for all $1 \leq m \leq M$. Similarly, it can be shown that \hat{f}_y is a consistent estimate of f_y under appropriate conditions on the partition (Lugosi & Nobel, 1999; Nobel, 1996). Then, $p_V(y^{\text{obs}})$ can be approximated by

$$\hat{p}_V(y^{\text{obs}}) = \sum_{m=1}^M p_m \mathbf{1}\{\hat{f}_m \leq \hat{f}_y(y^{\text{obs}})\}. \quad (15)$$

As for model (15), the coefficients p_m , for $m = 1, \dots, M$, can be approximated numerically to any arbitrary accuracy by simulating a large number of observations y and evaluating the proportion of them falling in each cell A_m .

3.3. Smoothing in observation geometry

In a satellite image, each pixel corresponds to a measurement of the incoming radiation flux in one direction, and atmospheric correction of the image is usually performed by processing each pixel independently of the others. This implies that, in this context, to process the whole image, one has to solve one inverse problem per pixel. More formally, the reflectance ρ in Eq. (6), as well as the operator Φ in Eq. (9), depend on three angles $t := (\theta_s, \theta_v, \Delta\phi)$ characterizing the observation geometry, namely the Sun zenith angle, the viewing zenith angle, and the azimuth difference angle (modulo π). Following Pelletier and Frouin (2004, 2005) and Frouin and Pelletier (2007), we start with a discretization of the domain T of observation geometries into N points t_1, \dots, t_N forming a grid in T . Next, for each discretization point t_i , with $1 \leq i \leq N$, the models defined in Section 3.2 are constructed. The inverse models corresponding to an arbitrary observation geometry t are then defined by interpolation of the models over the grid.

The interpolation procedure is similar for each type of inverse model and is detailed next for the retrieval of the marine reflectance. For any t in T , denote by $r_t(y)$ the condition expectation of x_w given y in model (9), where each quantity corresponds to the observation geometry t . Hence $\{r_t : t \in T\}$ is the collection of functions that are the Bayesian solutions formed when t varies in T . For each $1 \leq i \leq N$, we first construct the model \hat{r}_i associated with observation geometry t_i . Then, given the observation y^{obs} corresponding to the observation geometry t , the Bayesian solution $r_t(y^{\text{obs}})$ is approximated by

$$\hat{r}_t(y^{\text{obs}}) = \sum_{i=1}^N W_i(t) \hat{r}_i(y^{\text{obs}}). \quad (16)$$

In this equation, the coefficients $W_i(t)$, for $i = 1, \dots, N$, are defined in such a way that \hat{r}_t interpolates the N models \hat{r}_i , $i = 1, \dots, N$. As per the quality of approximation of this final model, for each fixed t in T , the error of approximation $\mathbb{E}\| \hat{r}_t(y) - r_t(y) \|^2$ can be made arbitrarily small since the joint distribution of (x_a, x_w, y) in Eq. (9) is known; its value depends first on the quality of each \hat{r}_i , $i = 1, \dots, N$, and second the number N of grid points for T , and the only limitations are the storage space for the model parameters and the execution time.

4. Modeling of the satellite signal

In this section, we provide details about the parameterizations, computations, and approximations used for the terms appearing in the decomposition of the satellite signal (Eq. 1), as well as a justification for this decomposition. In brief, the total signal is expressed as the sum of the marine signal (the signal of interest containing photons that have interacted with the water body) and the perturbing effects of the atmosphere and surface. Absorption by atmospheric gases is decoupled from scattering by molecules and aerosols and absorption by aerosols, and the water body is assumed to backscatter sunlight uniformly in all directions, i.e., the marine reflectance, ρ_{wv} , is independent of viewing geometry. Also, the effect of reflectance contrast between the surface target and its environment, referred to as adjacency effect, is not taken into account, which is equivalent to considering that the pixel size is infinitely large or that spatial variations in surface reflectance are not important (large target formalism generally used in ocean color remote sensing). Note that the errors introduced by the various parameterizations and simplifications, as well as other uncertainties in the radiative transfer modeling (e.g., treatment of the air-sea interface and aerosols) are taken into account in the Bayesian inversion via the term ε of Eq. (6).

4.1. Gaseous absorption

In Eq. (1), the effects of scattering by molecules and aerosols are decoupled from the effect of absorption by atmospheric gases, and the

gaseous transmittance is evaluated along the direct path from Sun to surface and surface to sensor. This is justified for ozone, which is located high in the atmosphere, where molecules and aerosols are rarified. Consequently, the incident and detected photons practically cross the ozone layer without being scattered. In the case of water vapor, the absorption bands occur where molecular scattering is weak, i.e., where aerosol scattering dominates. Since above 850 nm order 1 and 2 scattering events constitute the quasi-totality of the aerosol scattering signal, and since aerosols scatter mainly forward, the actual path followed by the photons does not differ much from the direct path Sun-to-surface and surface-to-sensor. The same approximation is less justified for oxygen and nitrous oxide, especially when considering the completely atmospheric terms ρ_{mol} , ρ_{aer} , and $\rho_{mol-aer}$ (since photons do not interact with the surface or water body), but it is sufficiently accurate when gaseous absorption is weak (Deschamps, Herman, & Tanré, 1983), which is the case in the spectral bands of ocean color sensors. Thus for measurements in spectral bands contaminated by gaseous absorption, T_g is expressed as:

$$T_g = \prod_i t_{g_i}(\theta_s, \theta_v, U_i) \quad (17)$$

where t_{g_i} and U_i are the transmittance and amount of gaseous absorber i , with t_{g_i} calculated for the direct path Sun-to-surface and surface-to-sensor. Analytical expressions are obtained for t_{g_i} in each spectral band, by fitting random exponential band models (i.e., Goody (1964) for water vapor and Malkmus (1967) for the other gases) modified to take into account the variations of temperature and pressure along the atmospheric path (Buriez & Fouquart, 1980).

4.2. Sun glint reflectance

The Sun glint reflectance ρ_g is considered spectrally flat (spectral dependence of the refractive index of water versus air is neglected) and computed as a function of wind speed, U , using the Cox and Munk (1954) model:

$$\rho_g = \pi G(U) R_{\text{Fresnel}}(w) / [4 \cos^4(\beta) \cos(\theta_v) \cos(\theta_s)] \quad (18)$$

where R_{Fresnel} is the Fresnel coefficient at the air-sea interface for the reflection angle w , β is the wave inclination, and G is the Gaussian slope distribution (depends on wind speed U) as given by Cox and Munk (1954). Dependence on wind direction is ignored. Wind speed is obtained from meteorological data. The above expression is not accurate for high values of ρ_g (i.e., $\rho_g > 0.01$) due to uncertainties on surface wind speed and intrinsic variability of Fresnel reflection on a rough surface.

4.3. Effective whitecap reflectance

The effective reflectance of whitecaps ρ_f is modeled as the product of the fraction of the surface contaminated by whitecaps, A , and the reflectance of whitecaps, ρ_{f_0} . For A , the empirical relation between A and wind speed U obtained by Koepke (1984) is used, i.e., $A = 2.95 \times 10^{-6} U^{3.52}$ where U is expressed in m/s. For ρ_{f_0} , the mean value of 0.22 measured by Koepke (1984) for combined patches and streaks (accounts for the thinning of whitecaps with time) is used with a spectral factor $f(\lambda)$ based on in situ and aircraft measurements (Frouin, Schwindling, & Deschamps, 1996; Nicolas, Deschamps, & Frouin, 2001). Thus ρ_f is computed as:

$$\rho_f = A \rho_{f_0} = 0.22 A f(\lambda) = \begin{cases} 0.65 \times 10^{-6} U^{3.52} \exp(-1.75(\lambda - 0.6)) & \text{if } \lambda \geq 0.6 \\ 0.65 \times 10^{-6} U^{3.52} & \text{if } \lambda < 0.6. \end{cases} \quad (19)$$

4.4. Water body reflectance

The radiance backscattered by the water body, after transmission across the interface, is assumed independent of direction, i.e., ρ_w is constant with respect to viewing geometry. In actuality, ρ_w exhibits some angular anisotropy, especially at large viewing and solar zenith angles (Morel & Gentili, 1993; Morel, Voss, & Gentili, 1995).

Our treatment is based on the premise that errors introduced by neglecting bidirectional effects on ρ_w are small compared with other atmospheric correction errors, i.e., those associated with the determination of the atmospheric reflectance ρ_a . Furthermore, taking into account bidirectional effects would have required knowing the scattering phase function of marine particles and their assemblages, but such knowledge is not comprehensive.

Spatial heterogeneity in the water reflectance is neglected in Eq. (1). This assumption, commonly made in ocean color remote sensing, may not be valid in the vicinity of land, clouds, and sea ice, or more generally in regions where the spatial water reflectance contrast is relatively high (Bélanger et al., 2007; Santer & Schmechtig, 2000). The adjacency effects in the TOA imagery can be estimated, however, from the spatial reflectance fields and atmospheric properties initially retrieved (i.e., in the large target formalism), then used to correct the TOA imagery before applying again the inversion scheme.

Water reflectance in the ρ simulations is taken directly from in-situ datasets acquired in a wide range of Case 1 and Case 2 situations (details are provided in Section 5). Using an average reflectance model for water reflectance would be restrictive (e.g., too rigid spectral constraints), and varying arbitrarily, even within observed boundaries, the parameters affecting water reflectance, i.e., backscattering and absorption coefficients, would not describe well natural variability, and might complicate the problem unnecessarily (some simulated cases may not be realistic).

4.5. Atmospheric transmittance, reflectance, and spherical albedo

The various atmospheric functions and interaction terms in Eq. (1), except gaseous transmittance (expressed analytically), therefore ρ_a and ρ in Eq. (5), are computed using a successive-orders-of-scattering code (Deuzé, Herman, & Santer, 1989; Lenoble, Herman, Deuzé, Lafrance, & Tanré, 2007). In the computations, unlike for water reflectance (see above), the aerosol characteristics are specified from models. This approach is justified for several reasons. On the one hand, the aerosol parameters of the forward model are generally not all available in existing archives (e.g., vertical distribution is often missing), and data, when they exist, are mostly from coastal or island sites, i.e., they do not represent well the open ocean. On the other hand, the objective is to retrieve water reflectance, not aerosol properties. In practice, after correction for T_g , the successive-orders-of-scattering code is run twice, once with aerosols and non-null water reflectance and once with only molecules and $\rho_w = 0$, and the second output is subtracted from the first to yield ρ .

Fig. 2 displays, as an example, simulations of $\rho_{toa}\cos(\theta_s)$ (no gaseous absorption) and $\rho\cos(\theta_s)$ in the spectral range 400–900 nm for various aerosol conditions and angular geometries. The atmosphere contains molecules and aerosols and is bounded by a wavy surface. The water body is assumed black, i.e., $\rho_w = 0$. The total signal, i.e., $\rho_{toa}\cos(\theta_s)$, exhibits a strong spectral dependence for relative azimuth angles of 90 and 180°, i.e., side and backscattering geometries, with values increasing rapidly with decreasing wavelength (Fig. 2, middle left and bottom left). This is explained by the influence of molecular scattering. For a relative azimuth angle of 0°, i.e., forward scattering, the spectral variation of $\rho_{toa}\cos(\theta_s)$ is much smaller, essentially due to the influence of Sun glint (Fig. 2, top left). The signal corrected for molecular effects, i.e., $\rho\cos(\theta_s)$, is much smaller in magnitude, for example about twice less at 500 nm for the geometries considered (Fig. 2, top right, middle right, and bottom right). In the case of forward scattering, ρ is negative

(Fig. 2, top right), all the more as the aerosol optical thickness is large, because ρ_g is large and the term $\rho_g(t_a - t_{mol})$ that appears in the expression of ρ_a is negative and t_a decreases as aerosol optical thickness increases.

5. Approximation of the forward operator

Constructing the inverse models requires multiple computations of the corrected TOA reflectance ρ in spectral bands of interest for our application, i.e., the SeaWiFS spectral bands centered at 412, 443, 490, 510, 555, 670, 765, and 865 nm. Of course, the construction scheme is general, and not restricted to a particular set of spectral bands. The angular grid, i.e., the Sun and view zenith angles, θ_s and θ_v , and the relative azimuth angle between Sun and view directions, $\Delta\phi$, are given in Table 1. The zenith angles are the Gauss angles in the successive-orders-of-scattering routine used to compute ρ . The range of angular conditions generally encountered in ocean-color remote sensing is covered, including observations in the Sun glint. As discussed later, the number of computations required to approximate the theoretical maps defined in Section 2.1 (i.e., conditional expectation, covariance, and p-value) will be of the order of the hundred of million points for each geometry. To keep the necessary computer time within reachable bounds, we first quantize the forward operator for each geometry, that is, we set up, once and for all, a data base stored on disk where ρ is evaluated at selected sampling points in the parameter space of atmospheric and oceanic variables. Next, to evaluate ρ at an arbitrary point, i.e., for an arbitrary state of the ocean and the atmosphere, the operator is approximated by interpolation. This yields a substantial gain, both in execution time and disk storage space, since the computational cost of running a radiative transfer code twice far exceeds the one of performing interpolation. Naturally there is a price to pay for this strategy, which results in an approximation error of the theoretical forward operator, i.e., the differences between actual computations with the radiative transfer code and the results from the interpolation procedure. That said, with properly chosen quantization points, located on a fine enough grid, the approximation error of the forward operator is intended to be small compared with the other sources of uncertainties and is accounted for via the noise term ε in Eq. (9).

Recall the notations from Section 2.3 where \mathcal{X}_a denotes the set of possible values for the vector of atmospheric parameters $x_a = (x_{a,1}, \dots, x_{a,d})$ with $x_a = (\rho_a(\lambda_i), T_a(\lambda_i), S_a(\lambda_i))$ at wavelength λ_i , for $i = 1, \dots, d$. Similarly, \mathcal{X}_w denotes the set of possible values for the vector of marine reflectance at wavelengths $\lambda_1, \dots, \lambda_d$. In the next section, x_a is expressed as a function Φ_a of a vector of parameters γ_a taking values in a set Γ_a , so that we have $\mathcal{X}_a = \Phi_a(\Gamma_a)$, and we define a discretization of Γ_a . Next, we define a discretization of \mathcal{X}_w based on in-situ data.

5.1. Atmospheric functions

5.1.1. Definition of Γ_a

The components of the parameter vector γ_a are the pressure, the wind speed, and the aerosol scale height, optical thickness, and type (i.e., model). The first five parameters take values in a closed interval of the real line. The last parameter, i.e., the aerosol model, refers to a convex combination of three basic types, namely Continental, Maritime, and Urban, whose optical properties are specified from WMO (1983). In this display, each aerosol mixture is parameterized by the mixing proportions of the three basic types, i.e., by a parameter $\alpha = (\alpha_1, \alpha_2, \alpha_3)$ of the respective proportions. The proportions α_i 's are comprised between 0 and 1 and sum to 1, so that the parameter space for α is the two-dimensional unit simplex, further denoted by \mathcal{S}^2 , of \mathbb{R}^3 , i.e.,

$$\mathcal{S}^2 = \left\{ (\alpha_1, \alpha_2, \alpha_3) \in \mathbb{R}^3 : \sum_{i=1}^3 \alpha_i = 1 \text{ and } \alpha_i \geq 0 \text{ for all } 1 \leq i \leq 3 \right\}. \quad (20)$$

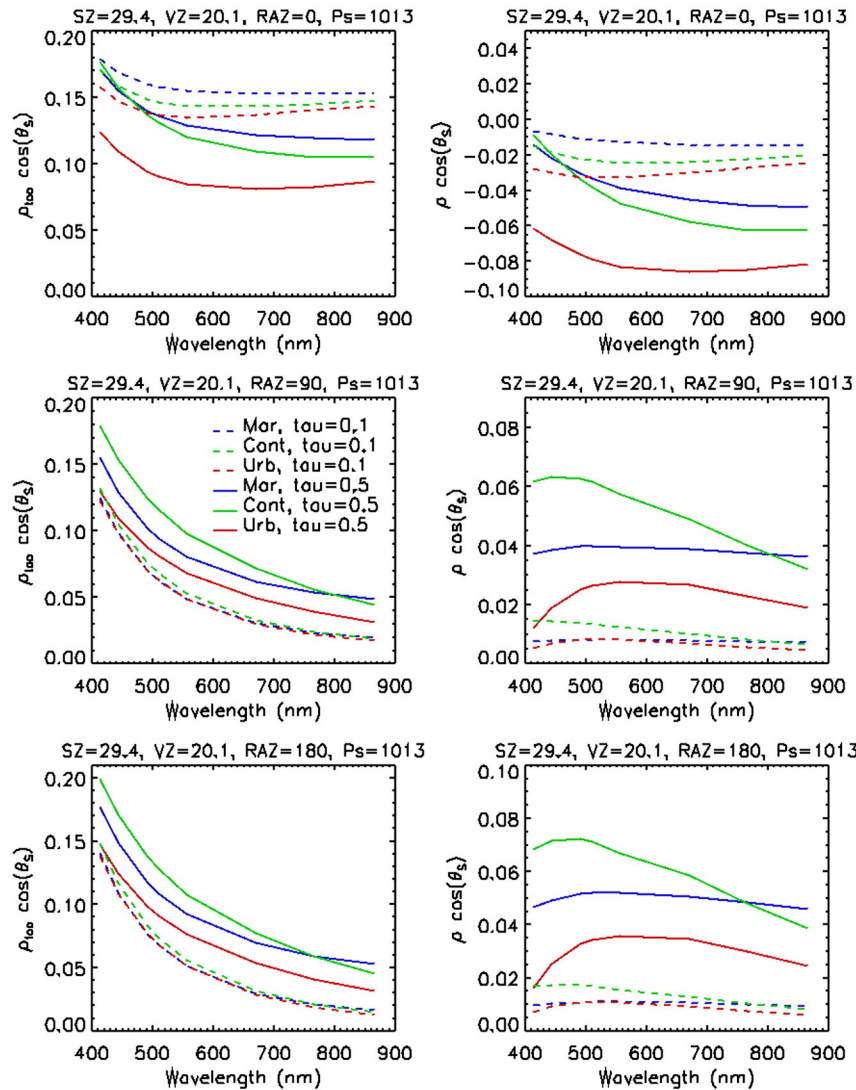


Fig. 2. Simulations of the top-of-atmosphere normalized radiance ($\pi L_{tot}/F_s$) by a vector radiation transfer code based on the successive-orders-of-scattering method. The atmosphere contains molecules and aerosols and is bounded by a wavy surface. Backscattering by the water body is null. Sun zenith angle is 29.4° , view zenith angle is 20.1° , relative azimuth angle is 0 (top panels), 90° (middle panels), and 180° (bottom panels), wind speed is 5 m/s, and surface pressure is 1013 hPa. Three types of aerosols are considered, i.e., maritime, continental, and urban, and aerosol optical thickness is 0.1 and 0.5 at 865 nm. Aerosol scale height is 2 km. The total signal is displayed in the left panels, and the signal after subtraction of the molecular signal (calculated assuming no aerosols) is displayed in the right panels.

This defines a set Γ_a as the product of five intervals times the 2-simplex \mathcal{S}^2 . The set Γ_a has been discretized by quantization points given in Table 2. For the aerosol models, the proportions have been set to mixtures of two basic types, with proportions varying by step of 20%. This corresponds to quantizing the boundary of \mathcal{S}^2 with 15 aerosol models.

We shall denote by \mathcal{R}_a the product of these five intervals, to arrive at the definition of Γ_a as $\Gamma_a = \mathcal{R}_a \times \mathcal{S}^2$, and we shall write any γ_a in Γ_a as $\gamma_a = (\zeta_a, \alpha)$ with ζ_a in \mathcal{R}_a and α in \mathcal{S}^2 . The set Γ_a is quantized into

$N = 6075$ points (see Table 2), and we end up with the database $\{(\gamma_{a,i}, \Phi_a(\gamma_{a,i})) : i = 1, \dots, N\}$ where the $\gamma_{a,i}$'s denote the N quantization points. Note that these computations are performed for the d wavelengths $\lambda_1, \dots, \lambda_d$ of interest.

5.1.2. Approximation of Φ_a

Write $\gamma_a = (\zeta_a, \alpha)$ with ζ_a in \mathcal{R}_a and α in \mathcal{S}^2 as above. Denote by $\{\zeta_{a,i} : i = 1, \dots, N_1\}$ the quantization points of \mathcal{R}_a , with $N_1 = 405$, and by $\{a_j : j = 1, \dots, N_2\}$ the initial quantization points of \mathcal{S}^2 , with $N_2 = 15$.

Table 1

Sun zenith angle, view zenith angle, and relative azimuth angle values of the grid.

θ_s, θ_v	0.11	1.43	3.28	5.14	7.00	8.87	10.73	12.59	14.46	16.32
	18.19	20.05	21.92	23.78	25.65	27.51	29.38	31.24	33.11	34.98
	36.84	38.71	40.57	42.44	44.30	46.17	48.03	49.90	51.76	53.63
	55.49	57.36	59.22	61.09	62.95	64.82	66.68	68.55	70.41	72.28
	74.15	76.01								
$\Delta\phi$	0.00	5.00	10.00	15.00	20.00	25.00	30.00	35.00	40.00	45.00
	50.00	55.00	60.00	65.00	70.00	75.00	80.00	85.00	90.00	95.00
	100.00	105.00	110.00	115.00	120.00	125.00	130.00	135.00	140.00	145.00
	150.00	155.00	160.00	165.00	170.00	175.00	180.00			

Table 2

Discretization of the atmospheric parameters space: sampling values, and number N of different values.

Parameter	Values	N
Pressure (hPa)	1003.0; 1013; 25; 1023	3
Aerosol scale height (km)	1.0; 2.0; 3.0	3
Aerosol models	15 WMO models; see text.	15
Aerosol optical thickness	0.0; 0.05; 0.1; 0.15; 0.2; 0.3; 0.4; 0.5; 0.6	9
Wind speed (m/s)	1.0; 3.0; 5.0; 8.0; 12.0	5

To approximate the value of Φ_a at (ζ_a, α) , we proceed by successive linear interpolations, first along ζ_a , and next along α . As a remark, proceeding the other way around (i.e., first along α and next along ζ_a) is equivalent for linear interpolation. Note first that \mathcal{R}_a is a product of closed intervals, and that the quantization points of \mathcal{R}_a are located on a regular grid. So in a first step, the values of $\Phi_a((\zeta_a, \alpha_j))$ are approximated by multilinear interpolation over \mathcal{R}_a for all $j = 1, \dots, N_2$. There remains to interpolate along the proportions α to approximate $\Phi_a((\zeta_a, \alpha))$. As a subset of \mathbb{R}^3 , \mathcal{S}^2 is isometric to an equilateral triangle in the plane. From the 15 quantization points on the boundary of \mathcal{S}^2 , we construct a regular mesh composed of 21 points, which form the vertices of 25 triangles whose union is \mathcal{S}^2 .

Successive linear interpolations between appropriate vertices of the mesh allow one to approximate the value of $\Phi_a((\zeta_a, \alpha))$ at an arbitrary α in \mathcal{S}^2 . The interpolation scheme is summarized in Table 3.

5.2. Marine signal

5.2.1. Definition of \mathcal{X}_w

Our goal here is to define an (approximately) uniform discretization of \mathcal{X}_w , that is, a finite collection of points of \mathcal{X}_w uniformly spread over \mathcal{X}_w . This could be achieved by considering several models relating the marine reflectance to biological parameters and/or inherent optical properties, but we find it more appropriate to base our analysis on in-situ measurements of the marine reflectance (see Section 3.1). We use measurements from the NOMAD dataset (Werdell & Bailey, 2005) and the AERONET-OC data archive (Zibordi et al., 2010).

The NOMAD dataset includes coincident measurements of marine reflectance and chlorophyll concentration compiled by the NASA Ocean Biology Processing Group (OBPG) from tens of field experiments. Above- and below-water radiometers are used in the measurement of marine reflectance. The major oceanic provinces are represented in NOMAD, but data are scarce in the southern Pacific and Indian Oceans, and in very clear waters. AERONET-OC provides marine reflectance and aerosol optical thickness through autonomous above-water radiometers operating on fixed platforms located near the coast. Situations of both Case I and Case II waters are sampled in NOMAD and AERONET-OC, but turbid waters containing sediments (e.g., from estuarine regions) are underrepresented in the ensembles.

5.2.2. The NOMAD data set

The NOMAD data set contains above 4000 measurements of the marine reflectance in 6 spectral bands from 412 nm to 670 nm (SeaWiFS spectral bands). Waters with chlorophyll concentrations in the range $0.01\text{--}100 \text{ mg m}^{-3}$ are represented. Due to lack of ancillary information, the measurements made by above-water instruments, which constitute

Table 4

Summary of NOMAD and AERONET-OC datasets of water reflectance. For NOMAD, the number of complete sets (i.e., measurements at the 6 shorter SeaWiFS wavelengths) are given in parenthesis. The data ensemble is composed of 21% cases from NOMAD (Case I waters only) and 79% from AERONET-OC (Case I and Case II waters). The Venice and MVCO sites, located in the Adriatic Sea and the Mid-Atlantic Bight, contribute most of the AERONET-OC data, i.e., 50 and 19%, respectively.

Site/dataset name	Latitude (°)	Longitude (°)	Nb. wavelengths	Nb. measurements
NOMAD	Variable	Variable	5 (6)	1722 (729)
Venice	45.31	12.50	8	6360
Abu Al Bukhoosh	25.49	53.14	8	614
COVE SEAPRISM	36.90	−75.71	8	467
Gustav Dalen Tower	58.59	17.46	8	920
Helsinki Lighthouse	59.94	24.92	8	731
Lucinda	−18.51	146.38	8	303
MVCO	41.30	−70.55	8	2311
Palgrundens	58.75	13.15	8	440
Wave CIS site CSI 6	28.86	−90.48	8	251

about 50% of the data set, were not corrected for anisotropy effects in the reflected light field, i.e., transformed to nadir values. The marine reflectance in the near infrared, i.e., at 765 nm and 865 nm, is not provided in NOMAD, but it is required for our analysis since we consider both Case I and Case II waters. While it is reasonable to assume a black ocean in the near infrared for Case I waters, this is not the case for Case II waters. In addition, the important variability in the observed Case II spectra makes it most difficult to reliably extrapolate the value of the marine reflectance at 865 nm, and even at 765 nm, based on measurements from 412 nm to 670 nm. Therefore from the NOMAD data set, the spectra identified as corresponding to Case I waters, and with at most one missing value, were extracted. This was accomplished using thresholds on the irradiance reflectance at 510 and 555 nm (Morel & Belanger, 2006). The number of extracted samples is equal to 2,651 and breaks down into 729 spectra without missing values, and 1922 spectra with at most one missing value, as summarized in Table 4. The value of these spectra at 765 nm and 865 nm is set to 0 under the black ocean assumption in the near infrared. Each missing value is then inferred from the complete data. The procedure for inference of the missing values, described below, has been limited to only one missing value per spectrum. In spite of the apparent regularity of Case I marine reflectance spectra, inferring strictly more than one missing value could not be achieved with enough confidence for our analysis. Most of the missing values are located in the spectral band centered at 670 nm. They can be estimated with reasonable confidence because of the relative regularity of the shape of Case I water spectra. That said, further inference, for more than one missing value, did not prove satisfactory for our analysis, which is the reason why Case I spectra with more than one missing value have been discarded from the NOMAD dataset.

Estimating the missing value in the marine reflectance spectra can be formulated as a regression problem, where the complete data is being used to fit a model predicting the value at the missing component. Numerous consistent regression estimation techniques exist. Among these, we use k -nearest neighbor estimates. We do not comment further on these aspects at this point and we refer the interested reader to Gyorfi et al. (2002) for an exposition of the theory. Additional practical

Table 3

Interpolation algorithm for the approximation of Φ_a .

Interpolation algorithm of Φ_a

- 1. Input:** The quantization points $\{\zeta_{a,i}; i = 1, \dots, N_1\}$ and $\{\alpha_j; j = 1, \dots, N_2\}$, the corresponding values $\Phi_a((\zeta_{a,i}, \alpha_j))$, and the evaluation point $\gamma_a := (\zeta_a, \alpha)$.
- For all $1 \leq j \leq N_2$, approximate $\Phi_a((\zeta_a, \alpha_j))$ by multilinear interpolation over \mathcal{R}_a using the values $\Phi_a((\zeta_{a,i}, \alpha_j))$, for $i = 1, \dots, N_1$, which gives the approximated values $\Phi_a((\zeta_a, \alpha_j))$.
- Form the regular triangular mesh of \mathcal{S}^2 , and approximate the value of Φ_a by successive linear interpolation based on the values estimated at step 2.
- Locate a triangle \mathcal{T} of the mesh containing α , and linearly interpolate at α using the values of step 3 located at the vertices of \mathcal{T} , yielding the approximated value $\Phi_a((\zeta_a, \alpha))$.
- 5. Output:** the approximated value $\Phi_a((\zeta_a, \alpha_j))$ of Φ_a at γ_a .

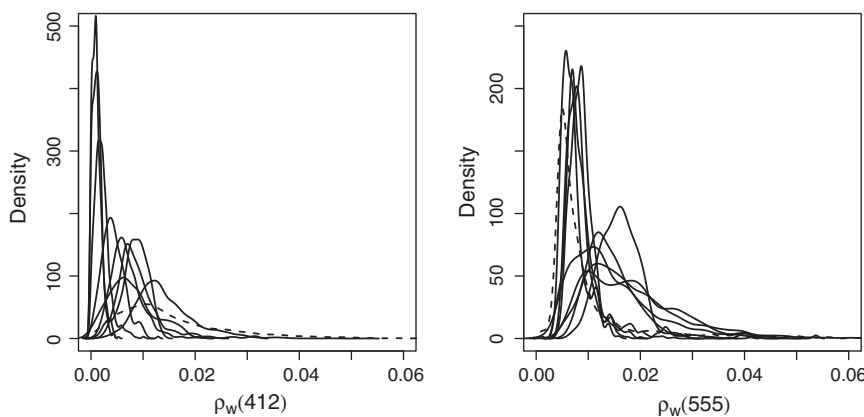


Fig. 3. Estimated densities of the marine reflectance at 412 and 555 nm, left and right, respectively, acquired at each of the 9 AERONET sites (solid lines) and assembled in NOMAD (dashed line).

implementation details are gathered in Appendix A at the end of the paper. The estimation procedure is repeated for each of the 6 channels where one value is missing, and this results in a complete data set of 2651 Case I marine reflectance spectra.

5.2.3. The AERONET-OC data sets

Marine reflectance data from 9 AERONET-OC sites listed in Table 4, collected during 2002 to 2010, were extracted from the online web archive. The data, in the form of normalized water-leaving radiance in 8 spectral bands centered at 413, 440, 501, 530, 555, 674, 870, and 1019 nm, were transformed into marine reflectance and corrected for directional effects, i.e., converted to values at nadir (see Zibordi et al., 2009). Splines were then used to generate marine reflectance at the SeaWiFS wavelengths. The total number of marine reflectance spectra is equal to 12,397, but the sample size varies significantly from one site to another, ranging from 251 points (Wave CIS CSI 6 site) to 6360 points (Venice site); see Table 4. In particular, about one half of the marine reflectance measurements come from the Venice site. The waters sampled have chlorophyll concentration in the approximate range 0.1–20 mg/m³, which is much smaller than the NOMAD range. Many of the spectra exhibit values that correspond to Case II waters, with relatively high values at 560 and 510 nm, and non-zero values in the near infrared. Statistical differences also exist between the time series acquired at different locations. As an example, the estimated densities of the marine reflectance at 412 nm and 555 nm at each site are plotted in Fig. 3, including those of the NOMAD data set. All the densities are essentially unimodal, but the location of the mode, as well as the spread, varies significantly with the geographical coordinates, i.e., water type or marine ecosystem. Narrow densities may be due, in some cases, to the limited amount of data at the stations. The larger spread is obtained with the NOMAD data set, presumably because it samples a wide range of chlorophyll concentrations and bio-geographic provinces.

5.2.4. Quantization of \mathcal{X}_w

The measurements from the 9 AERONET-OC sites, combined with measurements extracted from the NOMAD data set, constitute a total of 15,048 in-situ marine reflectance spectra, sampled from 412 nm to 865 nm. Only 21% of the cases are from NOMAD.

Because of sampling differences, the combined data points are not evenly distributed over the domain \mathcal{X}_w . Indeed, the extracted NOMAD data points are identified as corresponding to Case I waters, while the AERONET-OC data set covers both Case I and Case II waters. Moreover, from a statistical perspective, the NOMAD data come from separate field campaigns and can be considered as being roughly independent measurements. On the contrary, the AERONET-OC data come in the form of time series and are therefore naturally correlated. At last, the sample sizes of each group of data differ significantly. Note furthermore that the marine reflectance measurements were corrected for anisotropy in the light field, except the NOMAD above-water measurements (about 10% of the total ensemble). The forward model, on the other hand, assumes that the marine reflectance is isotropic (see Section 2.1). The solution of the inverse problem, therefore, will be a marine reflectance in the space defined by the NOMAD and AERONET-OC data sets (properly digitized, see below), i.e., a space of marine reflectance corrected for directional effects, under the assumption of isotropic marine reflectance. In actuality, i.e., using satellite observations, directional effects in the marine reflectance will introduce some errors in the retrievals.

To form a finite collection of marine spectra approximately uniformly distributed over \mathcal{X}_w we consider a standard accept/reject algorithm. More precisely, we first estimate \mathcal{X}_w by a union of balls centered at the in-situ data and with common radius. Next, we simulate an outcome of a random vector uniformly distributed over a rectangular domain containing all the balls. The simulated point is accepted if it belongs to one of the balls, and rejected otherwise.

This procedure is repeated until a number, fixed in advanced, of simulated points have been accepted. The in-situ data being fixed, this algorithm yields a set of simulated points uniformly distributed over the union of balls. It may be shown that this union of balls converges to the unknown set \mathcal{X}_w ; see e.g., Biau, Cadre, and Pelletier (2008).

Table 5

Prior distributions on the various parameters.

Parameter	Prior distribution
Pressure	Uniform over [1003, 1023]
Aerosol scale height	Uniform over [1.0, 3.0]
Aerosol model proportions	Uniform over the simplex S^2 .
Aerosol optical thickness	Log-normal
Wind speed	Uniform over [1, 12]
Marine reflectance	Uniform over \mathcal{X}_w

Table 6

Boundary values of the bins in the aerosol optical thickness at 865 nm. Each bin is of approximate equal probability according to the log-normal prior distribution. The total number of bins is 20.

0.0000	0.0158	0.0226	0.0288	0.0349	0.0412	0.0477
0.0547	0.0623	0.0707	0.0800	0.0905	0.1027	0.1170
0.1341	0.1555	0.1833	0.2222	0.2828	0.4046	0.6000

Table 7

Geometry-averaged statistics: bias and standard deviation per channel, averaged over all the observation geometries.

Wavelength (nm)	412	443	490	510	555	670
Average bias	1.81E-09	-8.06E-10	3.48E-09	3.06E-10	-1.08E-08	-4.66E-09
Average standard deviation	0.004321	0.003564	0.003220	0.002936	0.002652	0.001145

6. Practical implementation

6.1. Noise distribution

Let us recall model (9):

$$y = \Phi(x_a, x_w) + \varepsilon. \quad (21)$$

The additive term ε appearing in this model, referred to simply as the noise term, is intended to encapsulate all the sources of uncertainties in the forward modeling leading to Eq. (5). These include, in particular, measurement uncertainties, modeling uncertainties of the various radiative transfer processes, as well as the approximation error associated with the reconstruction of the forward operator by interpolation of the discrete (simulated) data. As stated in Section 3.1, we shall assume that ε is a Gaussian random vector with $\mathbb{E}[\varepsilon] = 0$ and $\text{Cov}(\varepsilon) = \sigma^2 \text{Id}_{\mathbb{R}^d}$. In this model, the parameter σ plays the role of the noise level in a deterministic setting.

Naturally this assumption is reductive. Indeed, modeling errors on the forward operator are likely to have a non-zero average (i.e., yielding a bias) and/or depend in magnitude on the input parameters (atmosphere and ocean states). Also, in a nonparametric setting,

i.e., without assumption on the distribution of ε , this latter cannot be inferred since ε is never observed (and nor are the variables x_a , x_w , and y measured simultaneously). It is therefore reasonable to impose a parametric assumption on the distribution of ε .

To determine a value of σ , we first extract N TOA reflectance y_1, \dots, y_N from various images acquired by the SeaWiFS sensor. Next, for each $i = 1, \dots, N$, let

$$\delta_i^2 = \inf \left\{ \|y_i - \Phi(x_a, x_w)\|^2 : (x_a, T_a, S_a) \in \mathcal{X}_a, x_w \in \mathcal{X}_w \right\}, \quad (22)$$

i.e., δ_i is the distance from y_i to $\Phi(\mathcal{X}_a, \mathcal{X}_w)$. Then, we define a value $\hat{\sigma}^2$ of σ^2 by averaging the δ_i^2 's, i.e., we set $\hat{\sigma}^2 = (1/N) \sum_{i=1}^N \delta_i^2$.

6.2. Prior distributions

By allowing one to quantify the frequencies of occurrence of the parameters of interest before the acquisition of the data to be inverted, a prior distribution represents a-priori information. When no such information is available to the user, one is frequently led to consider a uniform distribution over an appropriate set. In this study, we aim at implementing an atmospheric correction algorithm valid at a global

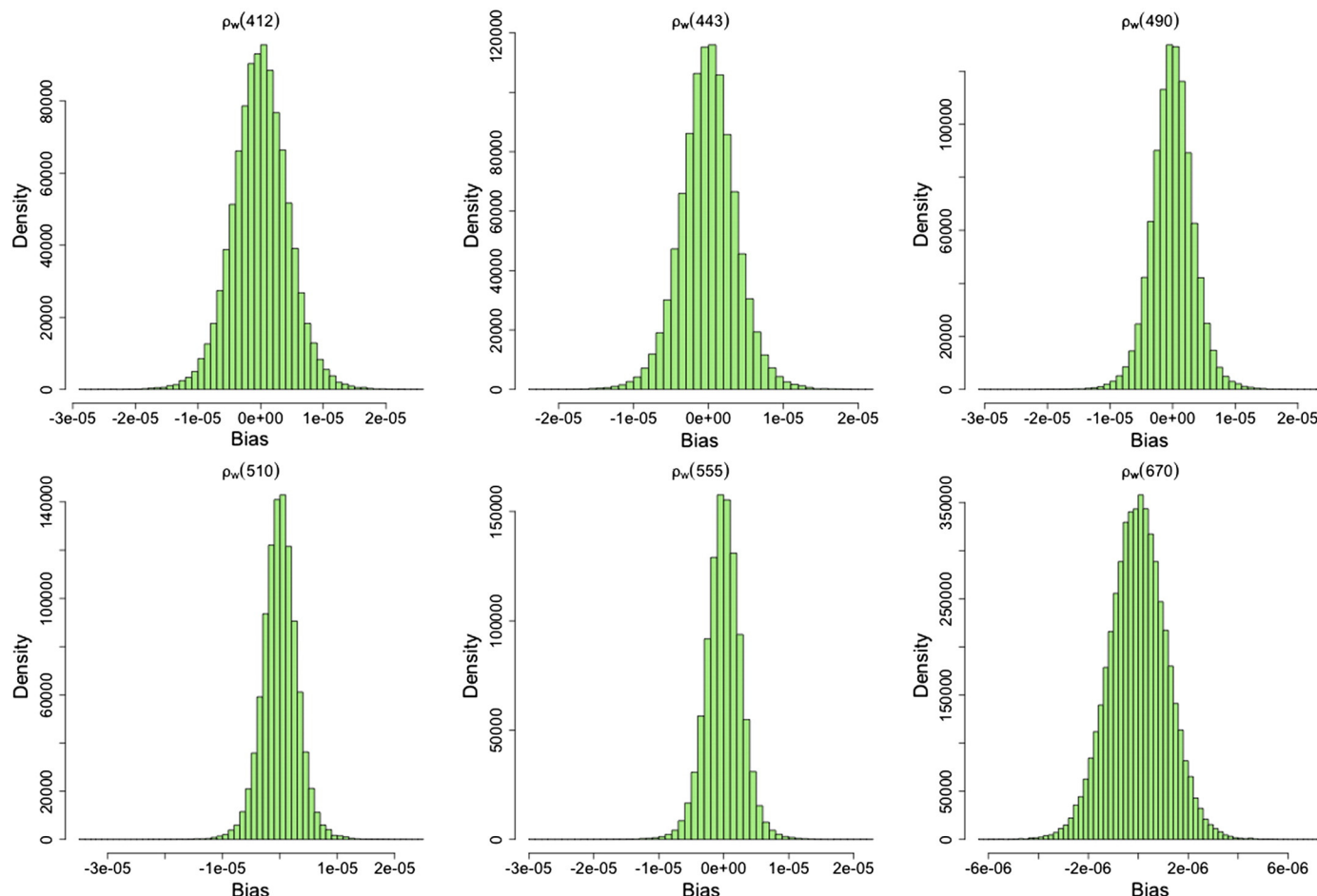


Fig. 4. Global statistics: histograms of the bias per wavelength.

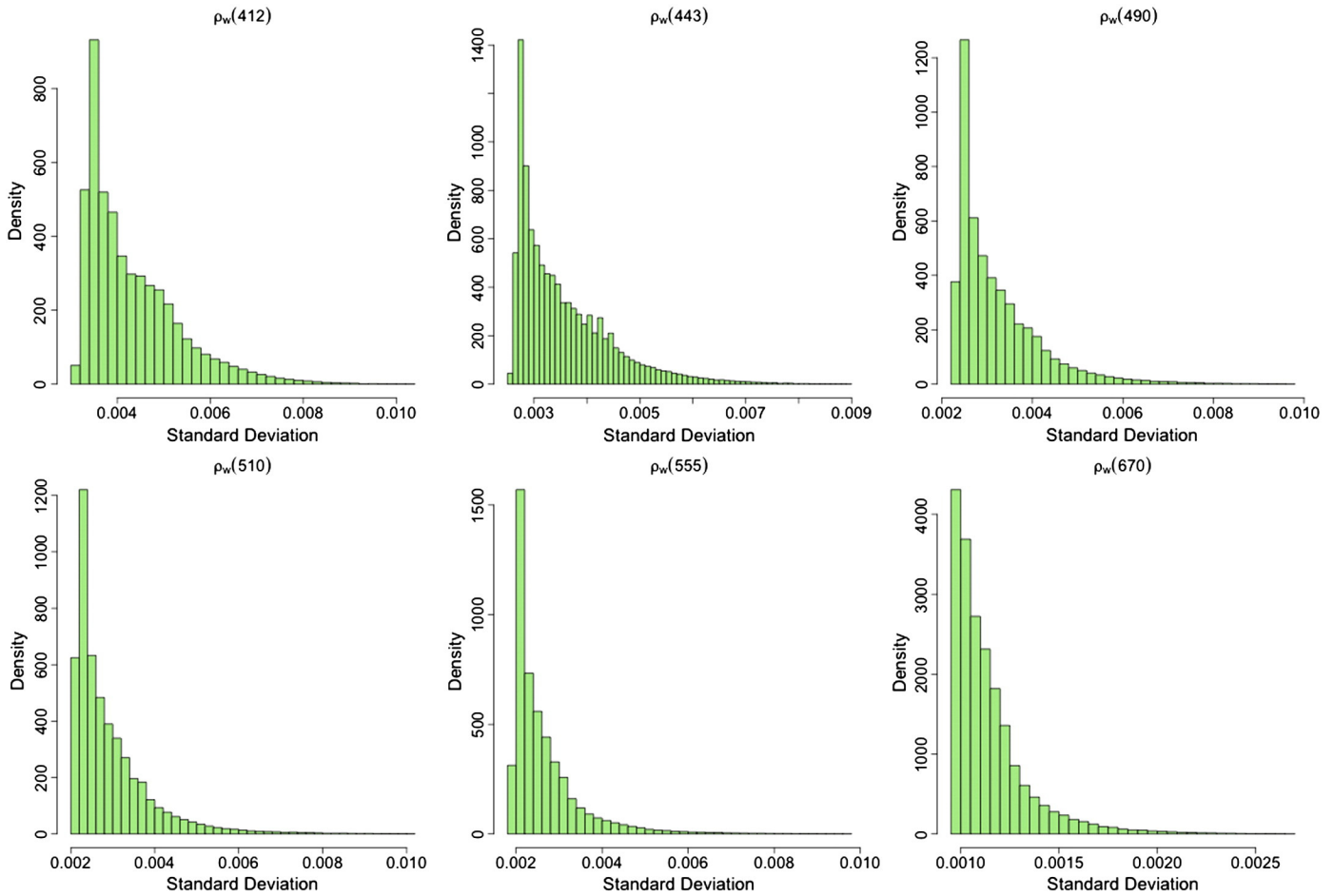


Fig. 5. Global statistics: histograms of the standard deviation per wavelength.

scale. For this purpose, a suitable prior distribution would have to reflect the frequencies of occurrence for parameters like the marine reflectance, or the aerosol optical thickness, at a global scale, global being meant both in space and time. In addition, since the prior distribution is one of the elements defining the Bayesian solution to the inverse problem, any information used to specify it must not originate from inversions of satellite observations, but instead from separate, independent field campaigns. As stated in Section 2.1, since there is no reason to expect, a-priori, that atmospheric and marine parameters should be correlated, the prior distribution on the parameter space $\mathcal{X}_a \times \mathcal{X}_w$ is of the product type $\mathbb{P}_a \otimes \mathbb{P}_w$.

The set \mathcal{X}_w has been defined in Section 5.2.1, and in the absence of other information, \mathbb{P}_w is taken as the uniform measure on \mathcal{X}_w . Recall that, in practice, we work with an (approximately) uniform discretization of \mathcal{X}_w in, say n , points $x_{w,1}, \dots, x_{w,n}$. So, in practice, we have $\mathbb{P}_w = \frac{1}{n} \sum_{i=1}^n \delta_{x_{w,i}}$ and sampling from \mathbb{P}_w simply amounts to selecting one of the $x_{w,i}$ uniformly at random and with replacement. Note that \mathbb{P}_w converges weakly to the uniform measure $U(\mathcal{X}_w)$ on \mathcal{X}_w as n goes to infinity; this means that, whenever n is large, the two measures \mathbb{P}_w and $U(\mathcal{X}_w)$ are close in some sense.

Using the notations from Section 5.1, we have $\mathcal{X}_w = \Phi_a(\Gamma_a)$, where $\Gamma_a = \mathcal{R}_a \times \mathcal{S}^2$, with \mathcal{R}_a being the joint parameter space for the pressure, wind-speed, aerosol scale height and aerosol optical thickness, and \mathcal{S}^2 , the 2-simplex, being the parameter space for the aerosol model. The study by Knobelspiesse et al. (2004) shows, from the analysis of 145 cruises in the Atlantic and Pacific oceans, and Asian seas (about 11,000 individual data points), that the aerosol optical thickness over the oceans is approximately distributed at the global scale as a log-normal

distribution. Hence we shall use this distribution as a prior distribution on τ_a with parameters taken as $\mu = -2.5257$ and $\sigma = 0.9854$ and extracted from Knobelspiesse et al. (2004). With these values for μ and σ , the 95% quantile is equal to approximately 0.40, which means that if one simulates values of τ_a from this prior distributions, then on average 95% of them will have a value lower than 0.40. For all the other parameters, to the best of our knowledge, no studies that are not based on satellite observations provide information on their relative frequencies at a global scale. Consequently, a uniform prior distribution of the domains of these parameters is retained. Formally, these considerations lead to defining a probability measure, say $\mathbb{P}_{a,0}$, on $\mathcal{R}_a \times \mathcal{S}^2$ as the product measure of several uniform distributions and a log-normal distribution. Then, this yields the prior distribution \mathbb{P}_a as the image of $\mathbb{P}_{a,0}$ through Φ_a , i.e., we have $\mathbb{P}_a = \mathbb{P}_{a,0} \circ \Phi_a^{-1}$.

The prior distributions are summarized in Table 5. Let us point out that, for the marine reflectance, considering a uniform prior distribution on \mathcal{X}_w already reflects a prior information, namely that values of the marine reflectance not belonging to \mathcal{X}_w are not realistic. This has been possible by using the in-situ data from the NOMAD archive and the various AERONET-OC sites. Naturally, since at a global scale most of the oceans are Case I waters, while only a small proportion corresponds to more optically complex waters, it may seem desirable to favor the first type of waters or, in other words, that the prior distribution on ρ_w places more weight on Case I ρ_w than others. How to do so in an objective way is a non-trivial matter at a global scale, for this would require extensive field campaigns to estimate reliably the frequencies of the marine reflectance. On the other hand, this may certainly be envisioned at a regional scale, a perspective which is discussed at the end of this paper.

6.3. Inverse applications

Recall the inverse models introduced in Section 3.2 for atmospheric correction, defined by:

$$\hat{r}(y^{\text{obs}}) = \sum_{m=1}^M (\alpha_m + B_m y^{\text{obs}}) \mathbf{1}_{A_m}(y^{\text{obs}}), \quad (23)$$

$$\hat{\Sigma}(y^{\text{obs}}) = \sum_{m=1}^M C_m \mathbf{1}_{A_m}(y^{\text{obs}}), \quad (24)$$

$$\hat{p}_V(y^{\text{obs}}) = \sum_{m=1}^M p_m \mathbf{1}\{\hat{f}_m \leq \hat{f}_y(y^{\text{obs}})\}, \quad (25)$$

where, for all $y \in \mathbb{R}^d$,

$$\hat{f}_y(y) = \sum_{m=1}^M \hat{f}_m \mathbf{1}_{A_m}(y) \text{ with } \hat{f}_m = \frac{p_m}{\text{Vol}_d(A_m)} \text{ and } p_m = \mathbb{P}(y \in A_m). \quad (26)$$

These models are all based on the same partition A_1, \dots, A_M of \mathbb{R}^d . Model (23) is an approximation of the conditional expectation $\mathbb{E}[x_{wl}|y = y^{\text{obs}}]$ given the observation y^{obs} ; it provides an estimation of the retrieved marine reflectance. Model (24) is an approximation of the conditional covariance $\text{Cov}(x_{wl}|y = y^{\text{obs}})$ given y^{obs} ; it provides a measure of uncertainty on the retrieved marine reflectance. Model (25) is an approximation of the probability that a new observation be at least as extreme as y^{obs} , in the sense of the definition given in Section 2.1; it can be used to detect cases where the forward modeling of the satellite

signal and the data y^{obs} significantly differ to the extent that the results of the inversion are meaningless.

In addition, and as a by-product, we also construct similar inverse models to retrieve the following atmospheric parameters: the term ρ_a in Eq. (9), the aerosol optical thickness, the aerosol model type (i.e., the proportions of the mixture), with accompanying uncertainties. Since retrieving these parameters is not the primary focus of this study, we use a simpler model than Eq. (1) where the linear model in each cell is replaced by a constant, i.e., each model is of the following generic form

$$\hat{r}_a(y^{\text{obs}}) = \sum_{m=1}^M \alpha_m \mathbf{1}_{A_m}(y^{\text{obs}}), \quad (27)$$

with coefficients $\alpha_1, \dots, \alpha_m$ in \mathbb{R}^p , where p denotes the dimension of x_a . The models for the conditional covariances are of the same type as Eq. (24).

6.3.1. Construction of the partition

Common to all the inverse applications defined above is a partition A_1, \dots, A_M of \mathbb{R}^d . To invert a reflectance y^{obs} , the first operation to be performed is to determine which one of the A_m 's contains y^{obs} . The computational cost to determining cell membership of an arbitrary partition can be very large, but it may be significantly reduced when the partition has an appropriate structure. To keep the execution of the inverse applications quick, we consider in this work a partition based on a perfect binary tree.

A tree is a hierarchical structure formed by a collection of linked nodes together with associated rules. The top node is called the *root* of the tree. Each node may have several *children nodes* and at most one *parent node*. Nodes without children nodes are called *leaves*, and the

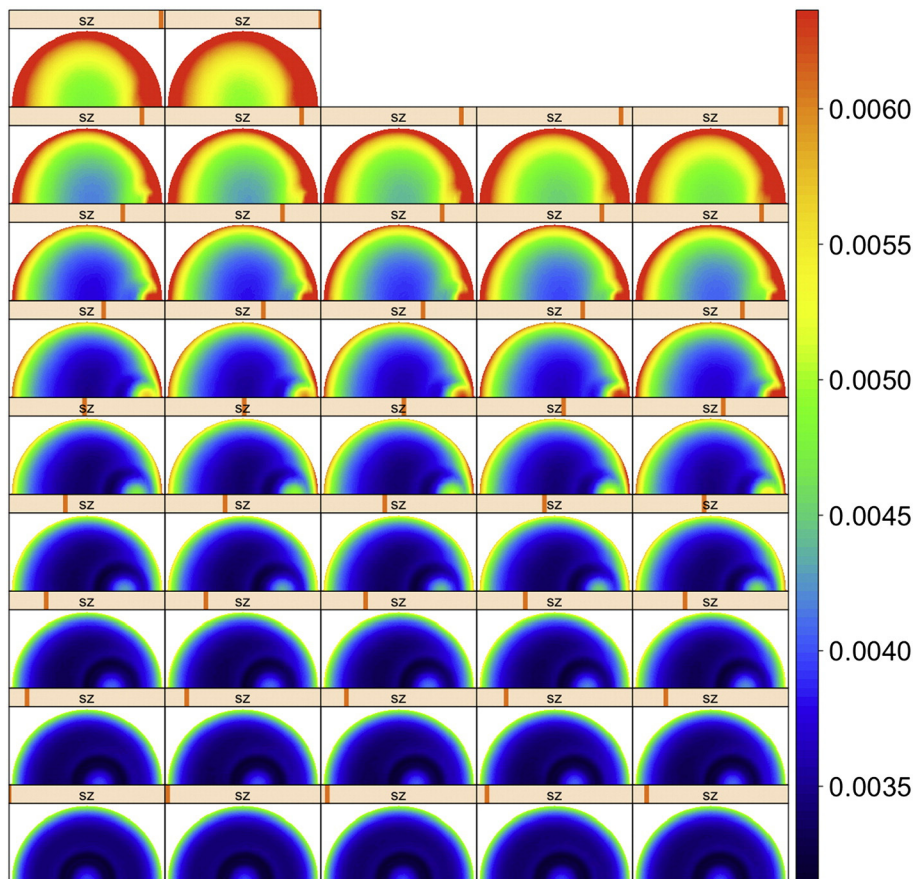


Fig. 6. Standard deviation per geometry at 412 nm. Each panel corresponds to a specific θ_s (from 0 to 76° , see Table 1), indicated by a vertical bar. The radius corresponds to $\sin \theta_v$ (with θ_v , like θ_s , from 0 to 76°) and the polar angle to $\Delta\phi$ (from 0 to 180°), with forward scattering to the right.

depth of a node is the length of the path from the root to the node. In a binary tree, each node has at most two children nodes. A binary tree is called *perfect* if every node other than the leaves has exactly two child nodes, and if all leaves are at the same depth. In this case, the two children of an internal node are commonly called the left and right children. The set of rules associated with the nodes other than the leaves induce a sequence defining paths from the root to the leaves. For our purposes, we consider binary comparison rules. Each rule is described by a pair (j, δ) , where j is an integer and where δ is a real number. To see how this effectively defines a partition, consider a vector y of \mathbb{R}^d , and denote by y_1, \dots, y_d its components. Starting from the root node, with rule (j, δ) , the j th component of y is compared with the threshold δ . If y_j is smaller than δ , then y is moved to the left child, otherwise, y is moved to the right child. The procedure is then repeated, either on the left child or on the right child, until the point y reaches a leaf. Hence this type of tree defines an axis-parallel partition of \mathbb{R}^d into hyper-rectangles: each cell of the induced partition is composed of the points y whose path in the tree attains the same leaf. So the resulting partition contains as many cells as leaves in the tree. In the case of a perfect binary tree, with depth K , the number of leaves is equal to $M = 2^K$. Note that, for an arbitrary point y of \mathbb{R}^d , the number of operations to perform to determine the cell to which y belongs is equal to K comparisons. We see then the strong computational interest in a tree-structured partition: the number of cells grows exponentially with the depth K , while the number of operations needed to determine cell memberships increases linearly with K . In addition, comparing two real numbers is computationally extremely fast.

In this work, we chose a depth $K = 17$ which yields $M = 2^K = 131,072$ cells. There remains to determine a set of splitting rules in such a way that convergence of the models is guaranteed. To this aim, we employ a fully data-driven procedure, i.e., the rules are determined

from a large number of simulated data y in model (9). Details of the algorithm are postponed to Appendix B at the end of the paper. For additional materials on this subject, we refer the reader to Breiman, Friedman, Olshen, and Stone (1984) and Breiman (2001) as well as Lugosi and Nobel (1999) and Nobel (1996).

6.3.2. Approximation of the model coefficients

From now on, the partition A_1, \dots, A_M is fixed and constructed as explained above. The optimal values for the coefficients $\alpha_m \in \mathbb{R}^d$, $B_m \in \mathcal{M}_d(\mathbb{R})$, $C_m \in \mathcal{M}_d(\mathbb{R})$ (a covariance matrix), and $p_m \in \mathbb{R}$, for $m = 1, \dots, M$, for the inverse applications (23), (24), and (25) are such that the L^2 risk is being minimized. Simple calculations allow one to derive their analytical expressions in terms of the joint distribution of (x_a, x_w, y) , which is known. In practice, their values are approximated numerically as follows.

Let $(x_{a,1}, x_{w,1}, y_1), \dots, (x_{a,n}, x_{w,n}, y_n)$ be n data simulated according to model (9). Next, the data is split among each element of the partition. In the following, for all $m = 1, \dots, M$, we set $\mathcal{I}_m = \{i = 1, \dots, n : y_i \in A_m\}$, and the number of points in \mathcal{I}_m is denoted by $\#\mathcal{I}_m$.

6.3.2.1. Marine reflectance models. For each cell A_m , the optimal coefficients $\hat{\alpha}_m$ and \hat{B}_m are approximated by minimizing the empirical risk $\sum_{i \in \mathcal{I}_m} \|x_{w,i} - \alpha - By_i\|^2$ over $\alpha \in \mathbb{R}^d$ and $B \in \mathcal{M}_d(\mathbb{R})$. The solution (not displayed here) can be expressed analytically; in practice, the optimal values are computed by fitting a linear model to the data $(x_{a,i}, x_{w,i}, y_i)$ with $i \in \mathcal{I}_m$, for all $m = 1, \dots, M$. For each $1 \leq m \leq M$, the covariance matrix \hat{C}_m is approximated by the empirical covariance, i.e., by $(\#\mathcal{I}_m)^{-1} \sum_{i \in \mathcal{I}_m} (x_{w,i} - \hat{\alpha}_m - \hat{B}_m y_i)(x_{w,i} - \hat{\alpha}_m - \hat{B}_m y_i)^t$.

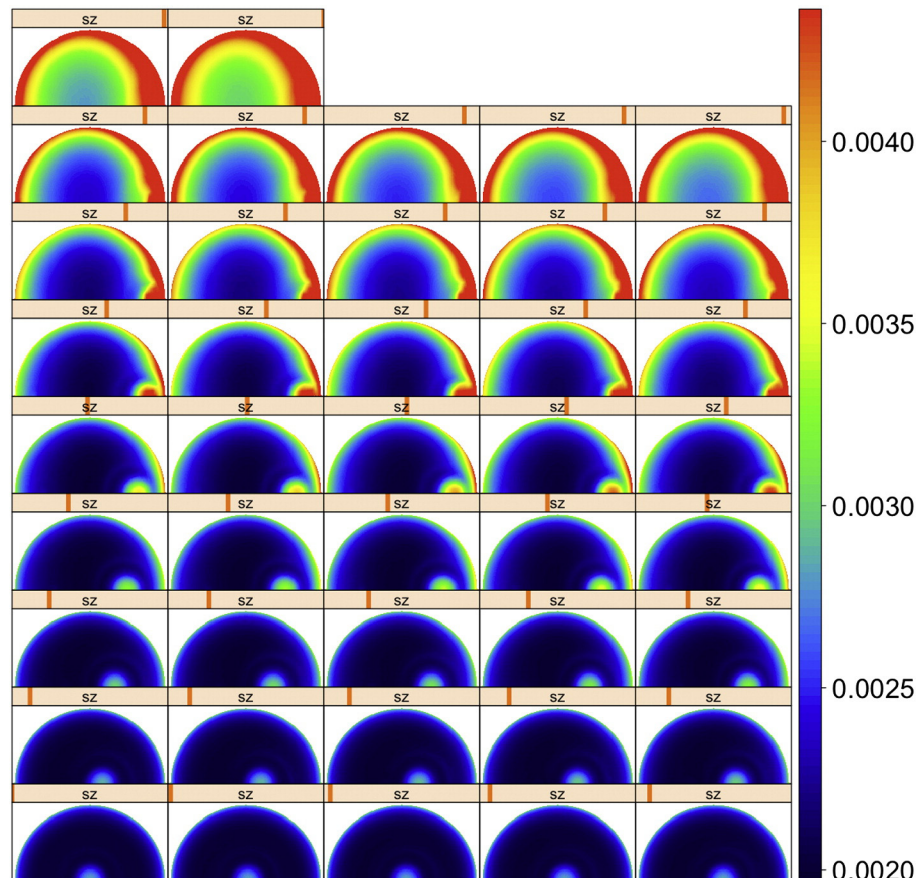


Fig. 7. Same as Fig. 6, but 555 nm.

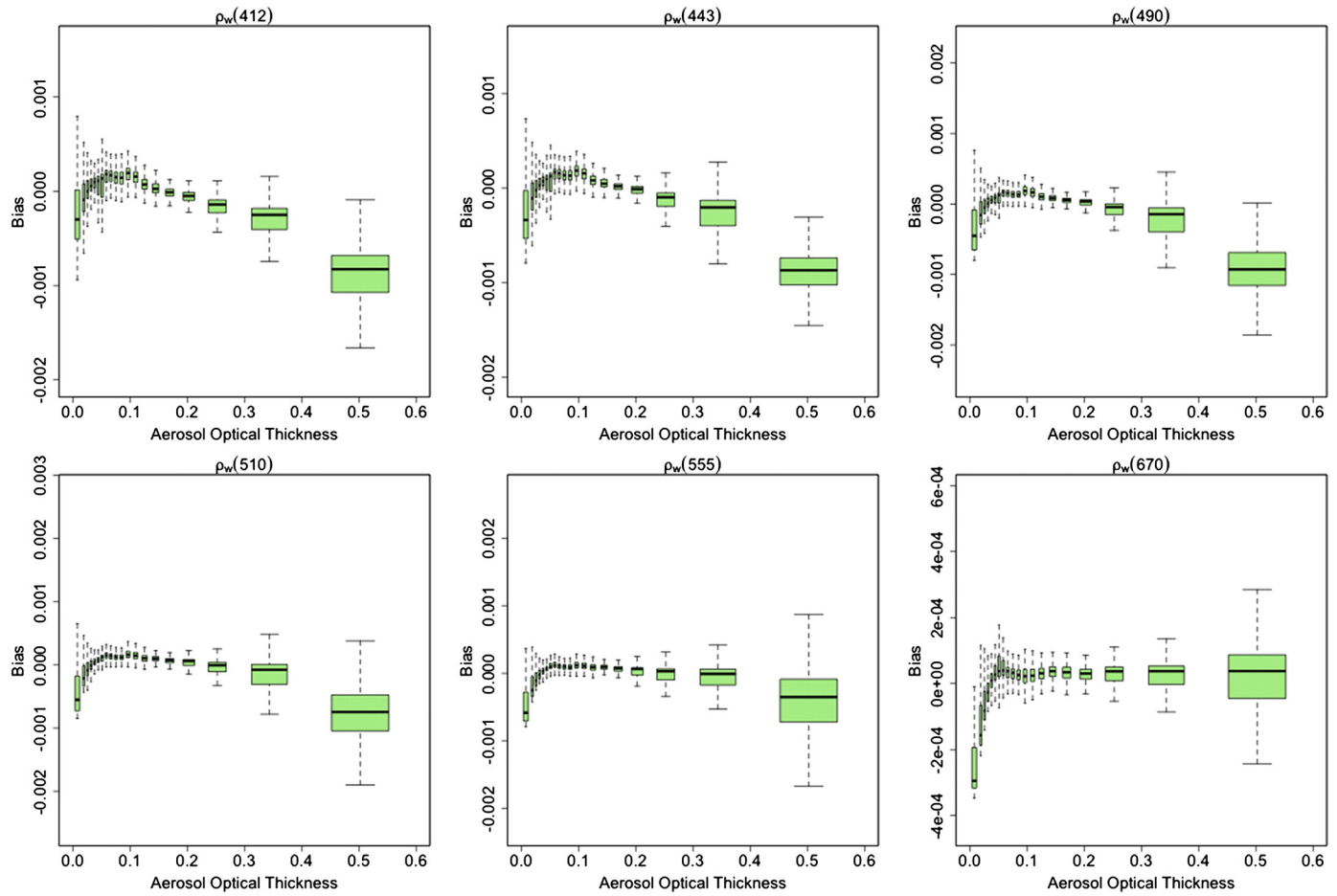


Fig. 8. Bias per spectral band and aerosol optical thickness bin, with all the geometries.

6.3.2.2. Atmospheric parameter models. For the retrieval of the atmospheric parameters, the models defined in Eq. (27) are simpler: these are constant functions on each A_m , $m = 1, \dots, M$. In this case, the optimal value $\hat{\alpha}_m$ for α_m is $\mathbb{E}[x_a | y \in A_m]$, which can be approximated numerically by the average of the $x_{a,i}$'s with corresponding y_i 's belonging to A_m , i.e., by $(\#\mathcal{I}_m)^{-1} \sum_{i \in \mathcal{I}_m} x_{a,i}$. As for the marine reflectance models, the optimal covariance matrix \hat{C}_m is approximated by the empirical covariance $(\#\mathcal{I}_m)^{-1} \sum_{i \in \mathcal{I}_m} (x_{a,i} - \hat{\alpha}_m)(x_{a,i} - \hat{\alpha}_m)^t$.

6.3.2.3. p-Value model. Two type of quantities have to be calculated to implement the model giving the *p*-value for the observation y^{obs} to be inverted, namely the volume $\text{Vol}_d(A_m)$ of the cell A_m , and the probability $p_m = \mathbb{P}(y \in A_m)$ that a new observation y falls in A_m , for each cell A_m , $m = 1, \dots, M$.

The volumes of the cells are computed at the time the partition is built. Note that, for the tree-structured partition, each cell A_m is the product of d intervals in \mathbb{R}^d . In theory, the cells can be unbounded. To cope with this issue, in practice, we first infer a hyper-rectangle \mathcal{B} , with sides parallel to the axes of \mathbb{R}^d which contains all the data points. Then we work with the intersections $A_m \cap \mathcal{B}$ in place of the cells A_m for volume computations. This does not change the theoretical properties of models (25) and (26) so this is not made precise in the definitions of these models for clarity.

At last, the probability that a new observation falls in the m^{th} cell A_m is approximated by the average number of points falling in A_m , i.e., by $\#\mathcal{I}_m/n$. Note that, by construction of the partition, these numbers are almost all equal to $1/(2^M)$, i.e., all cells have approximately equal probability by construction (see Appendix B).

7. Evaluation on simulated data

7.1. Performance statistics

To quantify performance, we consider the component-wise (i.e., per channel) biases, standard deviations, and mean squared errors defined respectively by

$$b_i = \mathbb{E}[\hat{r}_i(y) - x_{w,i}], \quad \sigma_i = \text{Var}(\hat{r}_i(y) - x_{w,i})^{1/2}, \quad \text{and} \quad \mathcal{E}_i = \mathbb{E}[(\hat{r}_i(y) - x_{w,i})^2], \quad (28)$$

for all $i = 1, \dots, d$. In these equations, the expectations are taken with respect to the distribution induced by the prior distributions and the noise distribution. The dependence of these quantities on \hat{r} is omitted in the notations. In what follows, the component-wise root mean squared errors (RMSE) refer to the $\mathcal{E}_i^{1/2}$. Also, note that $\mathcal{E}_i = b_i^2 + \sigma_i^2$, for all $i = 1, \dots, d$.

These quantities can be evaluated, theoretically, from the joint distribution of (x_a, x_w, y) since this latter is known. In practice, their values are approximated numerically by simulating a large number n of data according to model (9) and by replacing expectations with empirical averages in Eq. (28).

This procedure has been accomplished for each observation geometry configuration in the discretization of the angular domain (see the angular grid in Table 1) with a number n of 1 million points. We shall also consider the same statistics (i) by bins of aerosol optical thickness at 865 nm, and (ii) by bins of aerosol model proportions (in the 2-simplex). Formally, this amounts to replacing the expectations in Eq. (28) by conditional

expectations given the event that the aerosol optical thickness [for (i)] or the aerosol model [for (ii)] belongs to a given bin. As before, these quantities are approximated numerically by the same expressions, but from the part of the simulated data falling in the bin under consideration.

For the aerosol optical thickness, the boundary values of the bins have been taken as the quantiles of the prior distribution of orders an integer multiple of 5% (see Table 6), i.e., each bin is of equal probability for the prior log-normal distribution. Hence on average, each bin contains about 50,000 points. For the aerosol proportions, the 2-simplex is partitioned into 66 regular equilateral triangles of equal area, yielding 66 bins of equal probability according to the prior distribution, which we recall is the uniform distribution on the simplex.

The corners of each triangle defining a bin correspond to a mixture of the three basic aerosol types with mixture coefficients an integer multiple of 10%.

7.1.1. Average errors

In an attempt to provide a single measure of performance for the whole inversions, we defined a criterion by averaging biases and standard deviations over all the observation geometries; see the angular grid points in Table 1. Note that the grid points are Gauss angles, so they are not uniformly distributed. Also, the error statistics depend on Sun and view directions; some observation geometries are more favorable than others. Still, the sampling grid is finely defined, with well distributed grid points, so that the averaged statistics are a good measure of global accuracy.

Table 7 displays the bias and standard deviation per spectral band, averaged over all the geometries. The retrievals of the marine reflectance (ρ_w) are globally unbiased as expected; see the definitions in Eq. (28).

The average standard deviations vary from about 0.004 at 412 nm to 0.001 at 670 nm. This is acceptable, in view of the ρ_w mode values in the NOMAD and AERONET-OC data sets (see Fig. 3). The standard deviations would be smaller if unfavorable geometries (Sun glint, large air mass) were not included in the averages.

7.1.2. Errors per observation geometry

Figs. 4 and 5 display histograms of the average biases and standard deviations over the geophysical conditions of the simulated data set (each error composing the histograms corresponds to an individual geometry). It can be noticed that bias and standard deviation depend on the angles. The distribution of the biases appears to be centered and unimodal, with 95% of the values having a magnitude less than about 10^{-5} ($<3 \times 10^{-6}$ at 670 nm), i.e., the biases are small (Fig. 4). For the standard deviations, 95% of the values are below 0.007, 0.006, 0.006, 0.005, 0.005, and 0.002 at 412, 443, 490, 510, 555, and 670 nm, respectively (Fig. 5). Inversion errors, however, depend on the atmospheric parameters, as shown later in the analysis.

Figs. 6 and 7 display the standard deviations for each angular geometry at selected wavelengths, i.e., 412 and 555 nm. Biases are not shown since they are close to 0 (see Section 7.1), and they do not exhibit a noticeable dependence with Sun and view angles. Consequently, the RMSE is practically equal to the standard deviation, and dependence with geometry is almost the same. Each panel corresponds to a θ_s value of the angular grid (see Table 1). For each fixed value of θ_s , the (relative) viewing configuration is parameterized by a point in the upper half unit-disk of the plane. In polar coordinates, the radius corresponds to $\sin\theta_v$, while the angle corresponds to $\cos\Delta\phi$, with $\Delta\phi$ expressed in the convention of the successive-orders-of-scattering code, i.e., $\Delta\phi = 0^\circ$ for forward scattering and $\Delta\phi = 180^\circ$ for backscattering.

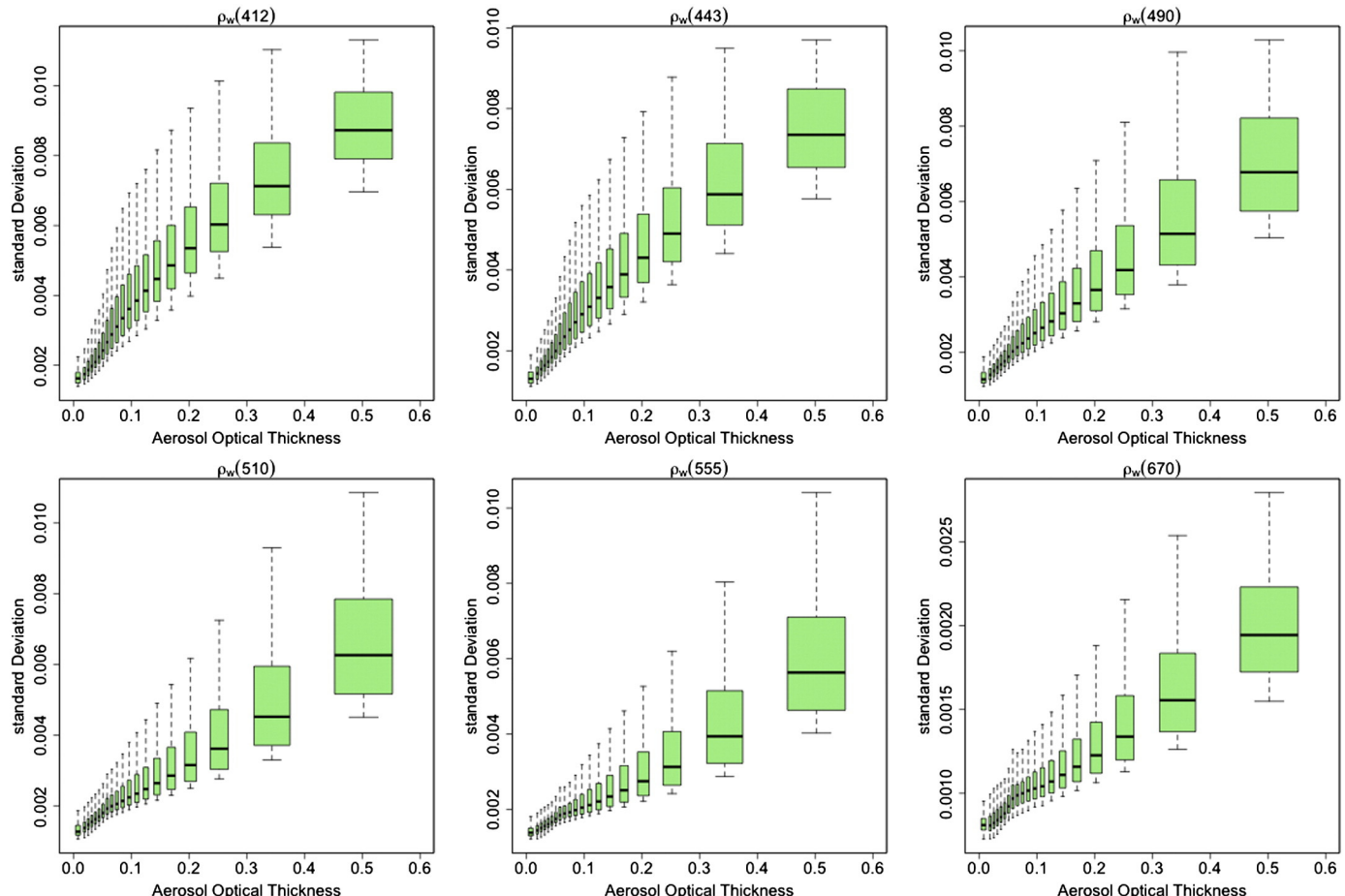


Fig. 9. Standard deviation per spectral band and aerosol optical thickness bin, with all the geometries.

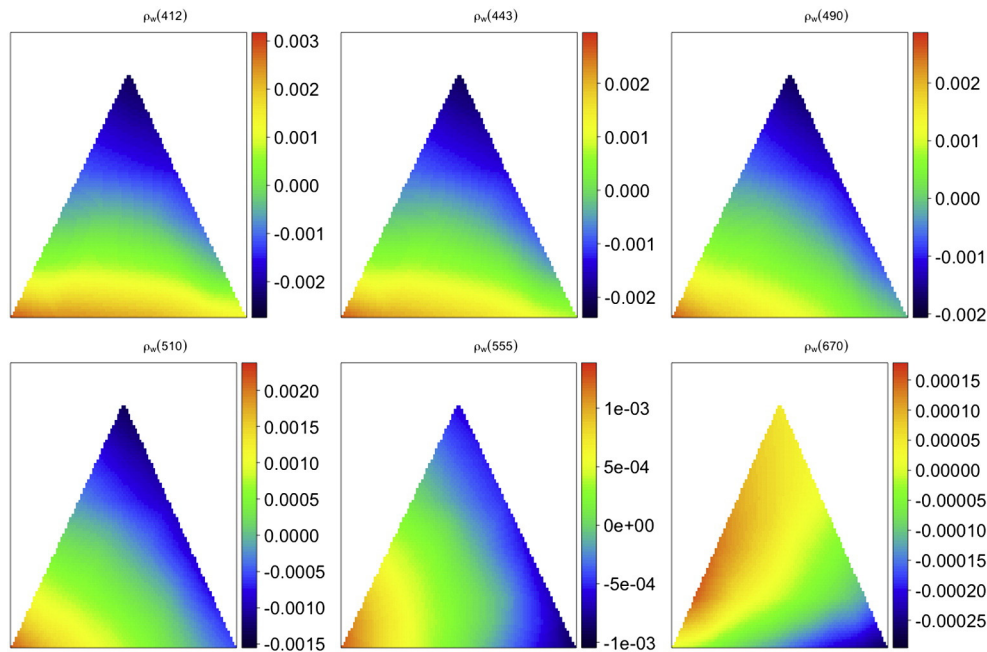


Fig. 10. Bias per spectral band, averaged over all geometries, as a function of the aerosol type. The top vertex corresponds to urban aerosols, the lower left vertex to continental aerosols, and the lower right vertex to maritime aerosols.

Error patterns are similar at the two wavelengths, but values are higher at the shorter wavelength (this is general when all wavelengths are considered). Outside the Sun glint region, standard deviation generally increases with air mass (larger ρ_a signal to correct). Small values are observed at large scattering angles ($>120^\circ$), where the aerosol phase function, i.e., the influence of aerosols, is relatively small. Inside the Sun glint region, performance is degraded, but remains reasonable (e.g., <0.005 at 412 nm) in many situations. At high Sun zenith angles (top three panels), the effect of Sun glint is less apparent, even absent, since it occurs at large view zenith angles, i.e., large air mass, for which the inversion is less accurate. Around the Sun glint directions, especially visible in the three lower panels, the standard deviation exhibits some of the smallest values. This is explained by the combined effect of a

large scattering angle in and around the Sun glint region and a relatively low air mass. The contrast between errors in the Sun glint and adjacent regions is sharp, because the presence of Sun glint is very sensitive to angular geometry (small changes in viewing direction may be associated with glint or no glint).

7.1.3. Errors per atmospheric parameter

7.1.3.1. Errors per aerosol optical thickness. The bias and standard deviation, averaged over all geometries, are displayed in Figs. 8 and 9 for each spectral band as a function of aerosol optical thickness bin at 865 nm (defined in Table 6). The box plots show that the bias is generally less than 0.0005 in magnitude, almost negligible at 670 nm. For

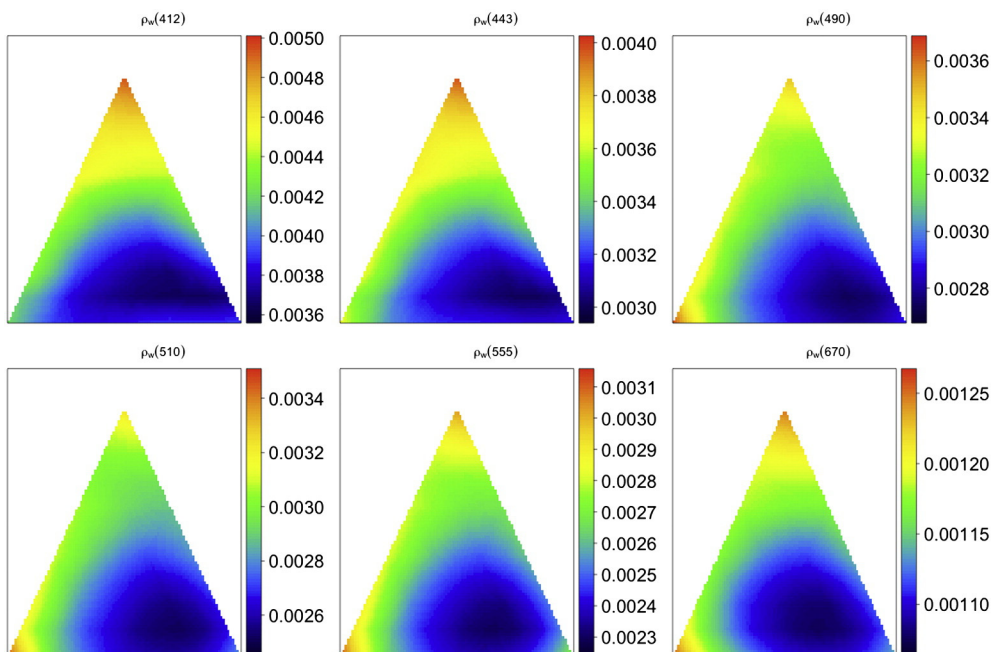


Fig. 11. Same as Fig. 10, but standard deviation.

large τ_a values (i.e., 0.4–0.6 bin), median absolute values reach 0.001 in the blue to yellow. The smallest biases are obtained for τ_a values of 0.05 to 0.15 (typically encountered in the open ocean). Below and above this value, biases are negative and positive, respectively. Standard deviation is generally higher at the shorter wavelengths and increases fairly linearly with aerosol optical thickness. The median value in the 0.4–0.6 τ_a bin reaches approximately 0.009, 0.006, and 0.002 at 412, 555, and 670 nm, respectively. In this bin, the sample maximum is above 0.01 at 412 and 555 nm, and about 0.003 at 670 nm. Errors are much lower at τ_a values generally encountered in the open ocean, for example 0.003, 0.002, and 0.001 at 412, 555, and 670 nm for τ_a equal to 0.1. Note that the standard deviation does not go to zero as τ_a decreases to zero because of the noise introduced in the data.

The influence of aerosol loading on the standard deviation varies with geometry. In fact, it can be modeled, at each wavelength, as a linear function of τ_a (not shown here). The fit is very good for most of the geometries. Departures from linearity occur at large sun zenith angles. The slope and intercept follow patterns similar to those in Figs. 6 and 7, with higher slope and intercept in the Sun glint region and at large air mass.

7.1.3.2. Errors per aerosol type. The bias and standard deviation, averaged over all geometries, are displayed in Figs. 10 and 11 for each spectral band as a function of aerosol type. In the triangles, values at the right, top, and left corners correspond to purely maritime, urban, and continental aerosols, respectively, values at the edges to proportions of two basic types, and values inside the triangles to mixtures of the three basic types (see Section 4 and the beginning of Section 5.1).

The bias is negative at all wavelengths for aerosol mixtures dominated by the urban type, except at 670 nm, where values are slightly positive. The situation is quite reversed for mixtures dominated by the continental

type, with positive bias at all wavelengths, except at 670 nm, where the bias is negligible. The mixtures dominated by the maritime type generally exhibit a small positive or negative bias. The standard deviation, on the other hand, is relatively small at all wavelengths when aerosols are mostly maritime, with minimum values occurring for mixtures of about 70% maritime, 15% urban, and 15% continental components.

The larger standard deviations are obtained for atmospheres with mostly urban or continental aerosols. The resulting RMSE (not shown) is also larger for those atmospheres, but due to the relative patterns of biases and standard deviations, the minimum values are shifted to mixtures containing 60% of maritime type. Note that the features in Figs. 10 and 11 are general, with slight variations from one geometry to the other.

7.1.4. Detailed analysis for a typical geometry

The inversion errors are examined for a typical geometry, i.e., $\theta_s = \theta_v = 30^\circ$, and $\Delta\phi = 120^\circ$. Fig. 12 displays estimated versus simulated (prescribed) ρ_w . The scatter plots indicate good performance at all wavelengths, with errors that do not depend significantly on the magnitude of ρ_w and sufficiently small to describe properly the variability of the simulated data set. In a few cases, however, the estimated values are inaccurate. This can be explained by the fact that these points lie close to the boundary of the support of the prior distribution of the marine reflectance. The biases are negligible and standard deviations are about 0.003, 0.002, 0.002, 0.001, 0.001, and <0.001 at 412, 443, 490, 510, 555, and 670 nm, respectively. These values are significantly lower than the globally averaged standard deviations reported in Table 7 (e.g., by 31% at 412 nm and 53% at 555 nm), for which all geometries are included. This illustrates the better performance for geometries typically encountered in ocean color remote sensing.

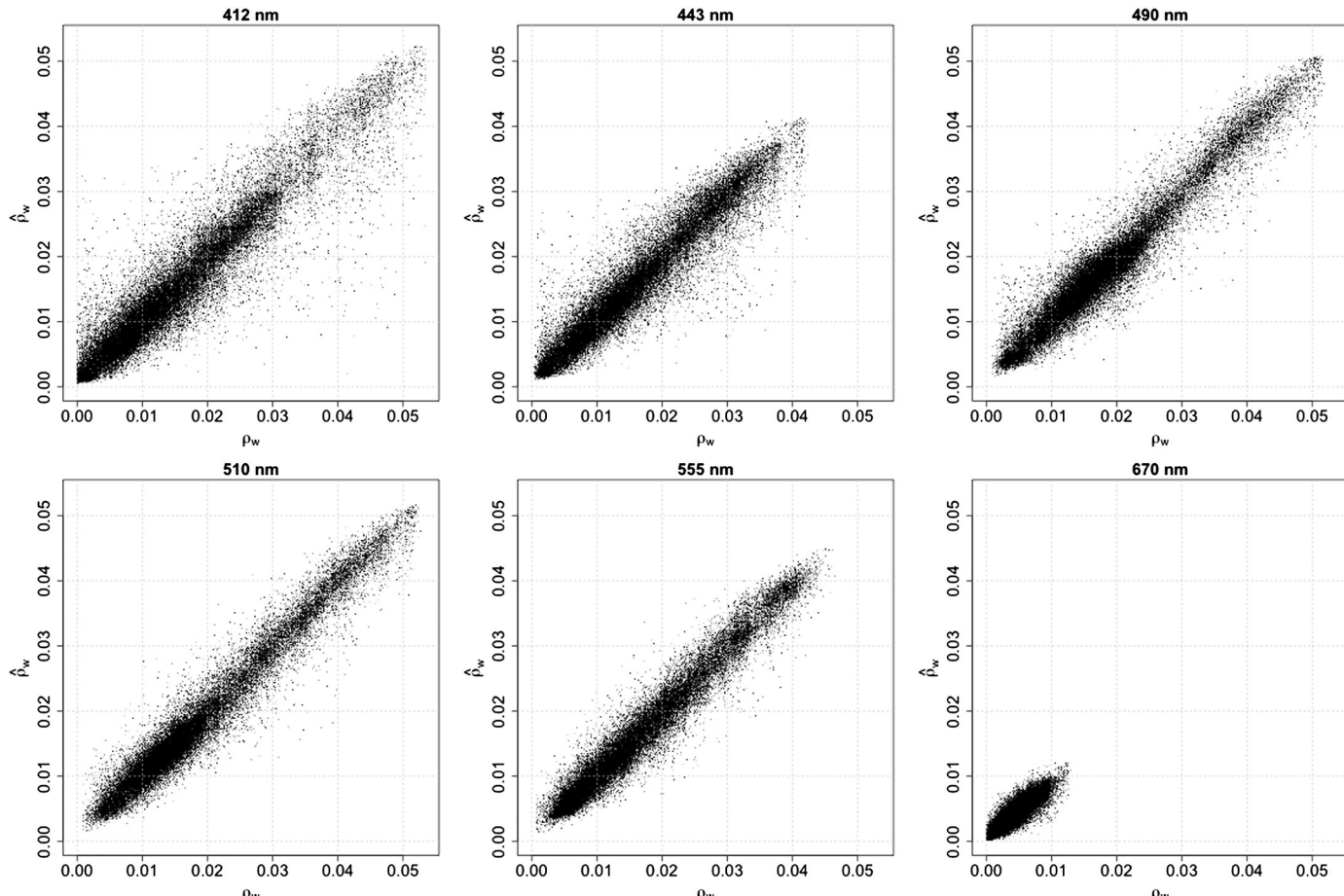


Fig. 12. Estimated versus simulated ρ_w in each spectral band, for a typical geometry (see text for details).

Fig. 13 displays for each wavelength the distribution of the total errors. About 70% of the cases have errors within the standard deviations indicated above. The estimated ρ_w standard deviation, a measure of uncertainty obtained from the posterior distribution, is plotted as a function of the ρ_w estimation error in **Fig. 14**. The estimated uncertainty remains within the lines of slopes $\pm 1/3$, i.e., within three standard deviations of the inversion error, indicating consistency with the inversion error.

Similar information is displayed in **Fig. 15** for τ_a , i.e., scatter plots of estimated versus simulated τ_a , histograms of inversion errors, and plots of estimated uncertainty versus inversion error. The conclusions for τ_a (as well as for ρ_a , not shown) are similar to those for ρ_w , i.e., accurate retrievals over the range of geophysical conditions considered with negligible biases on average, allowing a good description of variability, and estimated uncertainty coherent and compatible with inversion errors.

8. Application to SeaWiFS imagery

The Bayesian inverse methodology has been applied to actual SeaWiFS data. Reprocessing version R2010.0 was used, and no vicarious calibration adjustment was made to the data. Results are presented and discussed below for selected Local Area Coverage (LAC) imagery acquired over the ocean and seas around South Africa. The marine reflectance retrievals are analyzed in detail, including uncertainties, p -value, and spatial noise. Comparisons with estimates from the SeaDAS operational algorithm, are described. The Bayesian methodology is also evaluated against in situ water reflectance data collected in various oceanic regions.

8.1. S1999045100113 image, South Africa

Fig. 16 displays, for SeaWiFS imagery acquired on 14 February 1999 around South Africa, in the region of the Agulhas and Benguela Currents, Agulhas retro-reflection, and South Atlantic Current, the marine reflectance retrieved by the Bayesian inversion scheme in spectral bands centered on 412, 443, 490, 510, 555, and 670 nm. Clouds, masked using SeaDAS flags, are displayed in white. Near the coast, where upwelling brings nutrients to the surface, values are relatively low at 412, 443, and 490 nm and high at 555 and 670 nm near the coast (e.g., 0.005 at 443 nm and 555 nm), indicating productive waters. In the turbulent Agulhas retro-reflection zone (center of the image), marine reflectance in the blue is lower than in the surrounding regions of anti-cyclonic circulation associated with the Benguela drift (to the left) and the Agulhas return current (to the right), with values of 0.015 instead of 0.02 to 0.025. Near clouds, and in regions of broken cloudiness, the spatial features of marine reflectance exhibit continuity with respect to adjacent clear sky regions. No significant correlation exists between marine reflectance and wind speed, which exhibits a strong gradient from the center to the bottom of the image (not shown here), nor between marine reflectance and TOA reflectance at 865 nm. At the edge of the cloud system on the left of the image, for example, mesoscale eddies of relatively high marine reflectance are revealed, spatial features not apparent in the TOA reflectance at 865 nm (i.e., aerosol optical thickness) that exhibits a large gradient across the edge.

The absolute uncertainty associated with the marine reflectance estimates is provided in **Fig. 17** for each spectral band on a pixel-by-pixel basis. This uncertainty was calculated as the square root of diagonal elements of the covariance matrix of the conditional (posterior) distribution of ρ_w given ρ (see **Section 2.1**). For most pixels, values remain

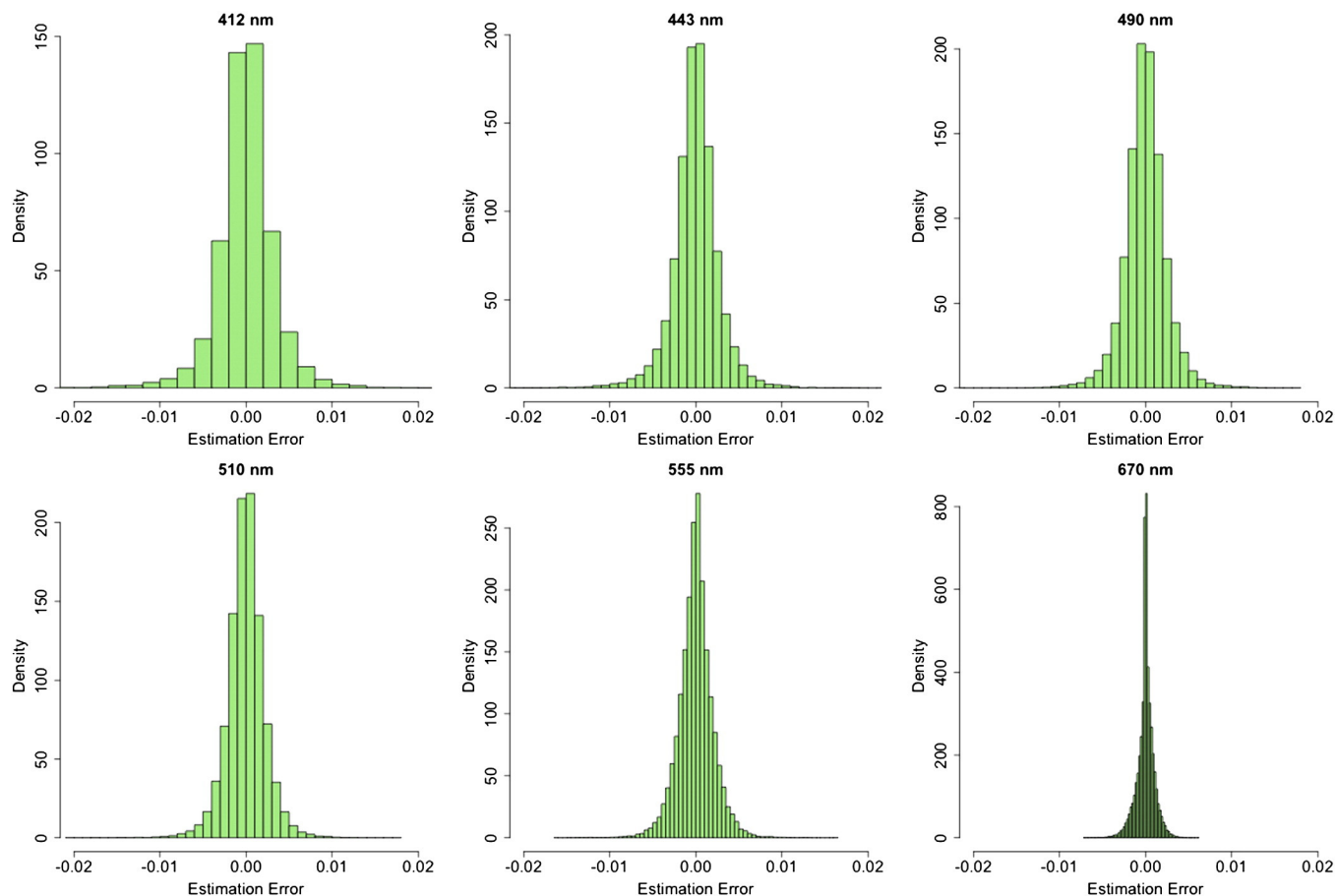


Fig. 13. Histograms of ρ_w estimation error.

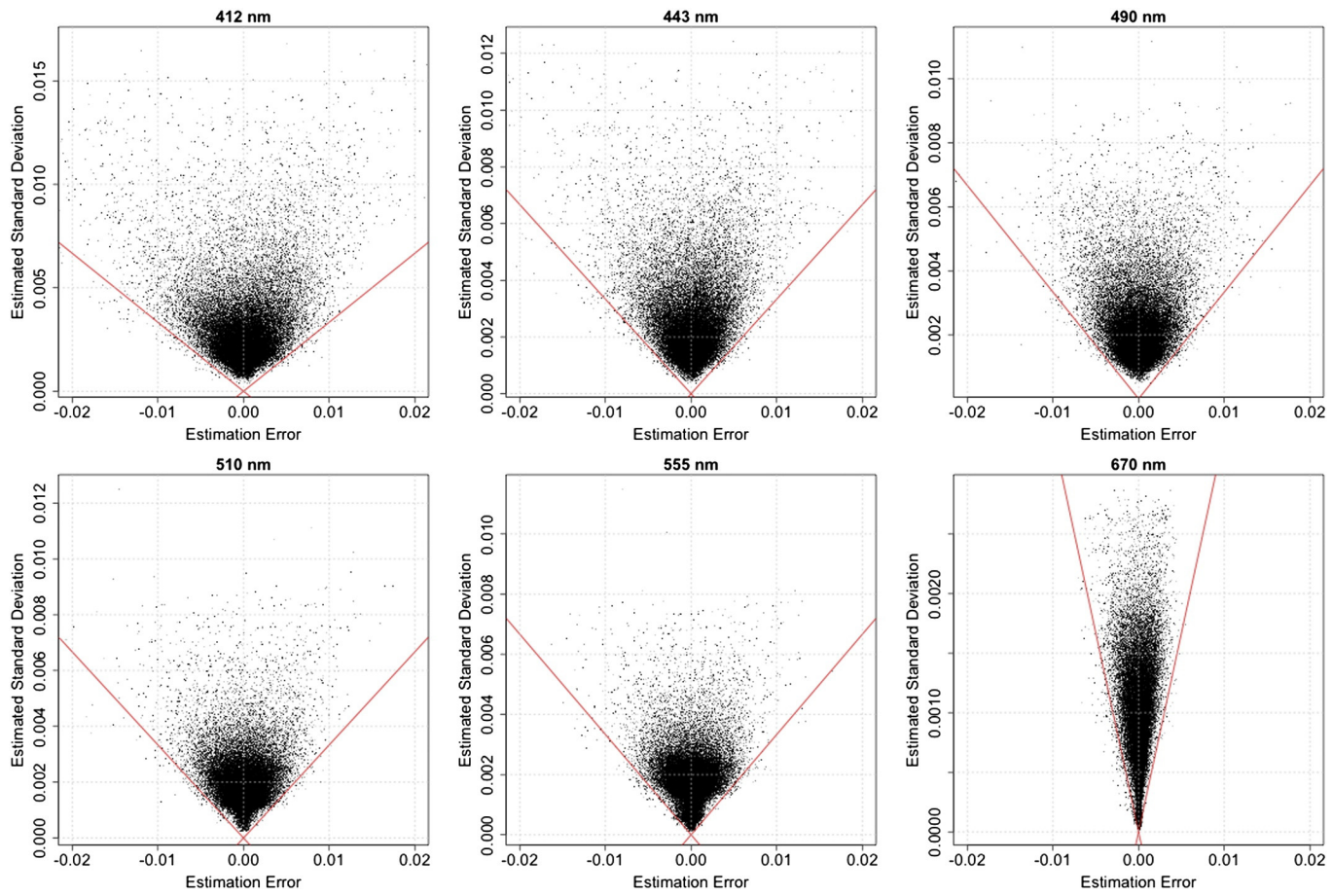


Fig. 14. Estimated ρ_w standard deviation versus ρ_w estimation error, with lines of slopes $\pm 1/3$.

within ± 0.003 in the blue, ± 0.002 in the green, and ± 0.0005 in the red. Larger uncertainties, i.e., ± 0.005 to ± 0.01 in the blue, are encountered near clouds (imperfect cloud masking or processes not accounted for in the modeling) and in regions where the TOA reflectance at 865 nm is large. The amplitude of the uncertainty is generally larger when the marine reflectance is higher. It corresponds to a percentage of the marine reflectance ranging between 40% (coastal regions) and 10% (outside the retro-reflection zone).

The marine reflectance fields obtained from SeaDAS, displayed in Fig. 18, exhibit spatial features showing resemblance in characteristics and appearance with the corresponding Bayesian fields. The marine

reflectance values are slightly smaller than the Bayesian estimates, but they vary within a similar range. More abnormal values are retrieved with SeaDAS near clouds, and the imagery is generally noisier. This is especially apparent in the marine reflectance field at 670 nm (Fig. 18 compared with Fig. 16, bottom right). The differences between the two types of estimates are also evidenced in the histograms of marine reflectance (Fig. 19), which show distributions similar in shape, but shifted toward higher values in the case of SeaDAS, by about 0.002 at 412, 443, 490 and 510 nm, 0.001 at 555 nm, and 0.0005 at 670 nm. At these last two wavelengths, the SeaDAS values are more broadly distributed, with peaks at 0.005 and 0.0007, respectively. Fig. 20 displays

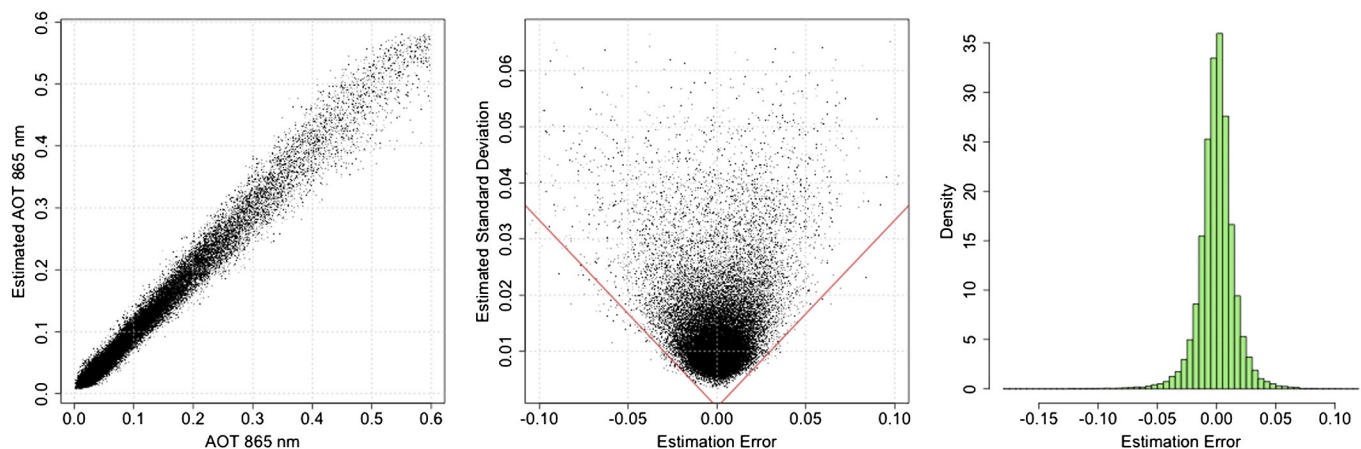


Fig. 15. (Left) Estimated versus simulated τ_a . (Center) Estimated τ_a standard deviation versus τ_a estimation error with lines of slopes $\pm 1/3$. (Right) Histogram of τ_a estimation errors.

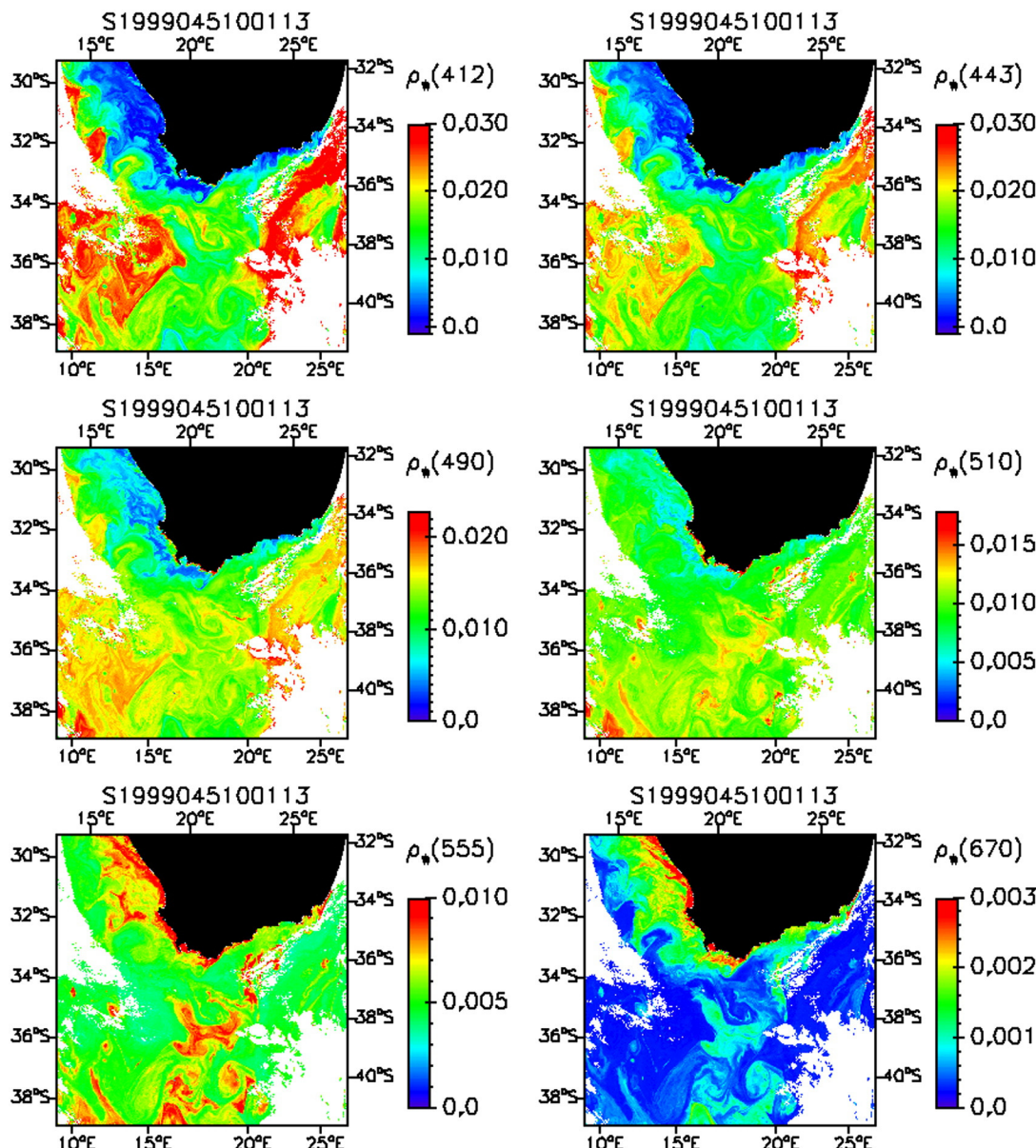


Fig. 16. Estimated ρ_w by the Bayesian methodology for SeaWiFS imagery of the ocean off South Africa acquired on February 14, 1999.

variograms of marine reflectance, obtained for a 128×128 pixel sub-area centered at about 18E and 36S. These variograms are defined as the variance of the difference between marine reflectance at two locations. They describe the degree of spatial dependence of the marine reflectance field. The SeaDAS values do not go to zero as spatial distance goes to zero, indicating more noisy retrievals. This may be attributed to the aerosol model selection in the SeaDAS algorithm (different models selected for neighboring pixels). Spatial correlation is lower at small scales with SeaDAS, and tends to decrease more slowly as distance increases. The differences have consequences on the determination of de-correlation scales and analysis of mesoscale ocean biological variability (see, e.g., Doney, Glover, McCue, & Fuentes, 2003).

The Bayesian technique retrieves not only marine reflectance, but also aerosol optical thickness τ_a and the atmospheric term ρ_a (see Eq. 5) at all wavelengths. Fig. 21 displays τ_a and ρ_a at 865 nm and their associated uncertainties. The τ_a values range from 0.02 to 0.2 and the ρ_a values from 0.001 to 0.015. High values are encountered near the edge to the cloud system off the West Coast of South Africa and in the immediate vicinity of clouds, and they correspond to high TOA

reflectance values at 865 nm. As expected the fields of τ_a and ρ_a are well correlated, since ρ_a is essentially proportional to τ_a . The uncertainty on τ_a and ρ_a is generally within ± 0.01 and ± 0.0005 , with higher values in regions of relatively high aerosol optical thickness (e.g., upper left part of the image).

The p -value associated to each pixel of (or retrieval in) the image is also displayed in Fig. 21. As explained in Section 3.1, this parameter quantifies how likely is the observation ρ with respect to the model. A low p -value (i.e., < 0.01 or 0.05) indicates that model and observation are incompatible. The p -value in Fig. 21 is above 0.05 almost everywhere, except in the vicinity of clouds, where some processes may not be accounted for in the radiation-transfer modeling (e.g., adjacency effects due to the high reflectance contrast between clouds and the environment, large optical thickness). Low p -values are also encountered where winds are especially strong, i.e., in the region between the Cape of Good Hope and the Southeastern part of the cloud system in the upper left part of the image, where wind speed exceeds 12 m/s. Such conditions are outside the atmospheric parameter space used for approximating the forward operator Φ_a (see Section 5.1).

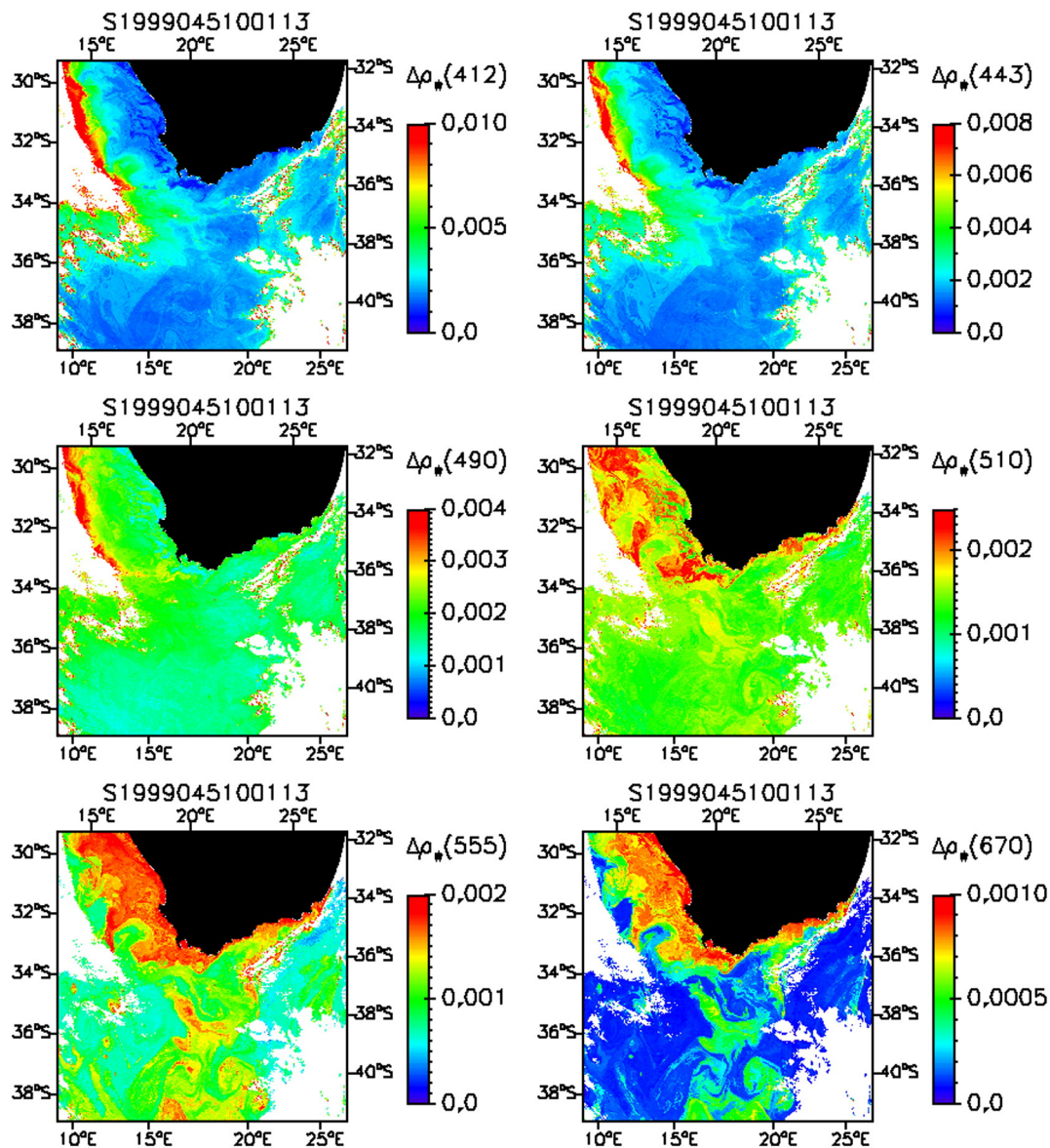


Fig. 17. Same as Fig. 16, but estimated ρ_w standard deviation.

8.2. Comparison with in-situ data

The performance of the Bayesian technique has been evaluated experimentally in comparisons with in situ measurements of marine reflectance. The measurements were taken from the MOBY and NOMAD data sets (Clark et al., 2003; Werdell & Bailey, 2005) and matched with the satellite data, within ± 3 h of overpass. The closest 3×3 pixel box was selected for processing by the inversion scheme, and the marine reflectance retrieved for each of the 9 pixels was interpolated to the geographic location of the in situ measurements. The cases for which some of the pixels in the box did not pass the SeaDAS cloud-screening flags were eliminated. This treatment, however, may not be sufficient when clouds are within a distance of 10 km, due to adjacency effects (Santer & Schmechtig, 2000). The TOA radiance was not corrected for absolute vicarious calibration adjustment (only temporal calibration changes were taken into account), allowing the MOBY data to be considered in the evaluation. Note that the NOMAD data can be included in the comparisons because they were only used in the model specification to define the support of the prior distribution on the marine reflectance. The match-up data set is not used in the construction of the models.

The marine reflectance match-up data sets covered the period from September 1997 to March 2004 (NOMAD) and December 1997 to March 2007 (MOBY), and consisted of 690 and 948 pairs of estimated and measured values, respectively. These included 132, 144, 144, 113, 129, and 28 pairs at 412, 443, 490, 510, 555, and 670 nm for NOMAD and 158 pairs at each of the 6 wavelengths for MOBY. Sun zenith angle varied from 3 to 58°, view zenith angle from 22 to 58°, and relative azimuth angle from 75 to 180°, i.e., the match-up data encompassed a wide range of geometry conditions. Fig. 22 gives the geographic location of the match-up data. Most of the points are located between 60S and 60N in the Atlantic and Pacific Oceans, and in coastal regions of the United States, but the Indian Ocean and the Mediterranean Sea are also sampled. Oligotrophic (e.g., Tropical Pacific) to productive (e.g., Patagonia shelf, Benguela current) biological provinces, Case 1 and Case 2 waters are represented in the match-up data, as well as various types of aerosols, (e.g., maritime in the open ocean, continental and pollution-type in coastal regions).

Fig. 23 displays scatter plots of estimated versus measured marine reflectance for the MOBY and NOMAD data sets (left and right, respectively), and Tables 8 and 9 give the comparison statistics, in terms of coefficient of determination r^2 , bias (estimated minus measured values)

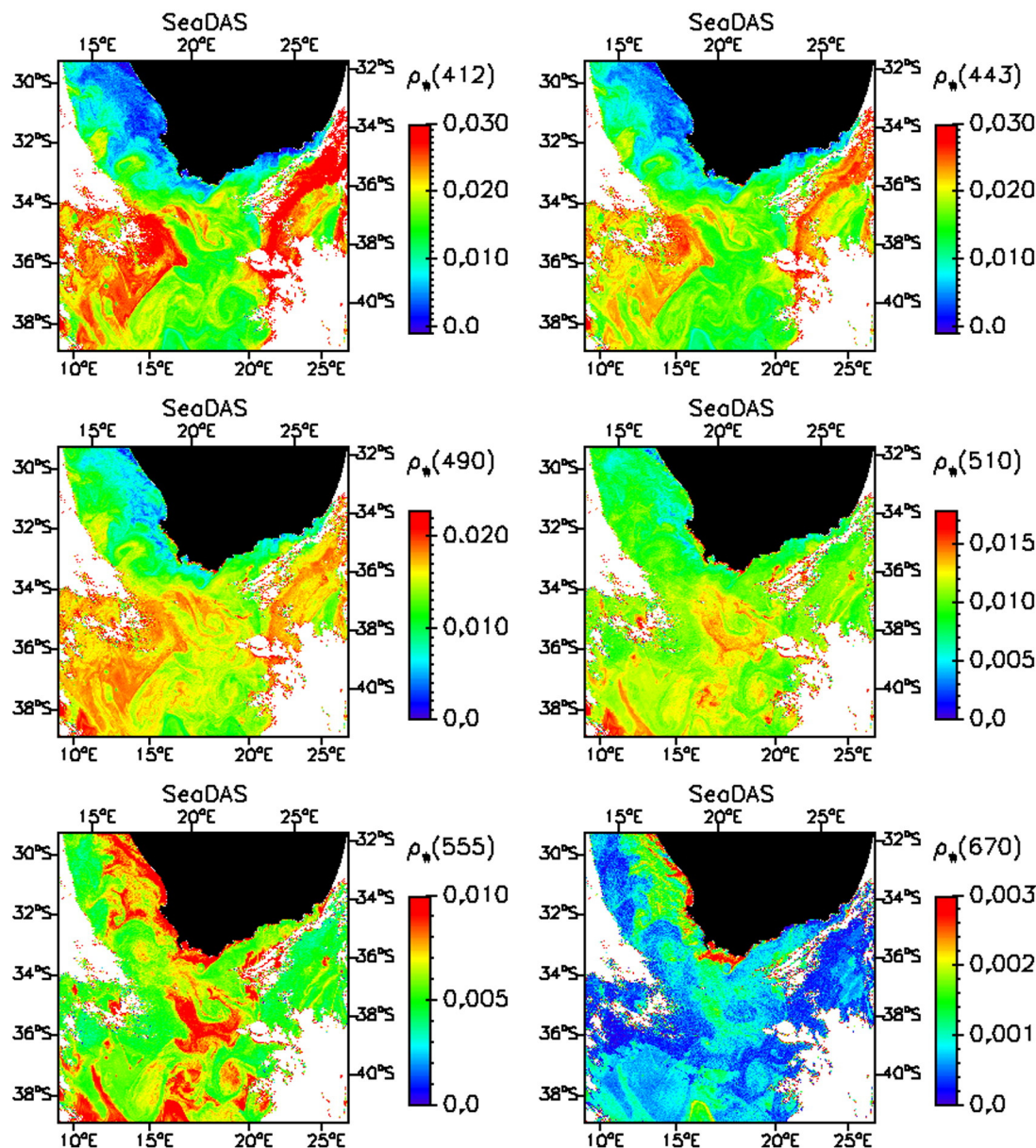


Fig. 18. Same as Fig. 16, but estimated ρ_w by the SeaDAS algorithm.

and RMS difference. In the scatter plots, the uncertainties associated with the marine reflectance retrievals are also displayed.

For the comparison using MOBY data (Fig. 23, left), the scatter is relatively small, but the Bayesian estimates are biased high at 412, 443, and 490 nm, by 0.004, 0.002, and 0.001, respectively (Table 8). This may be explained in view of the theoretical performance (Section 7) and the aerosols prevailing at the MOBY site. According to Smirnov, Holben, Dubovik, Frouin, and Slutsker (2003), at the Lanai AERONET site, located just a few kilometers from MOBY, the Angstrom exponent α characterizing the spectral dependence of the aerosol optical thickness between 400 and 870 nm ($\tau_a \approx \lambda^{-\alpha}$) exhibits an average value of about 0.7. This would correspond in our modeling to a mixture of WMO maritime and continental aerosols since these aerosols have an Angstrom exponent of 0.1 and 1.2, respectively (urban aerosols are unlikely in Lanai). For such mixtures, Fig. 13 indicates that positive biases, by a few 0.001, are expected theoretically. These biases may be reduced by algorithm regionalization, i.e., by taking into consideration a priori information on the aerosol properties prevailing in the region considered, which can be obtained from measurements or simulations from atmospheric transport models (see next section). Note, however, that the Bayesian

estimates and the measurements generally agree within uncertainties, as determined from the posterior distribution. At 443 nm, the RMS difference is 0.003 or 9.2%, which falls a bit short of the requirements of 0.001–0.002 or 5% in clear waters for biological applications (Gordon, 1997). At 510, 555, and 670 nm, the r^2 values are small, due to the lack of variability in the marine reflectance (Case 1, oligotrophic waters).

For the comparison using NOMAD data (Fig. 23, bottom), the Bayesian estimates are less biased in magnitude than when using MOBY data, but the scatter is larger. The biases (higher Bayesian values) are 0.002 or 7.8% at 412 nm, 0.001 or 5% at 443 nm, and smaller at the other wavelengths (<0.0001 at 670 nm) (Table 9). They represent a small component of the RMS errors, which decrease from 0.0059 at 412 nm to 0.0026 at 555 nm and to 0.0012 at 670 nm. Similar performance is obtained using the SeaDAS algorithm, with RMS errors of 0.0054 at 412 nm, 0.0028 at 555 nm, and 0.0019 at 670 nm. The RMS errors on the Bayesian estimates are also comparable with those computed for the SeaDAS algorithm by the NASA OBPG using a much larger match-up data set sampling a wider range of conditions (4577 points), i.e., 0.0075 at 412 nm, 0.0045 at 555 nm, and 0.0019 at 670 nm (details are available on the OBPG web

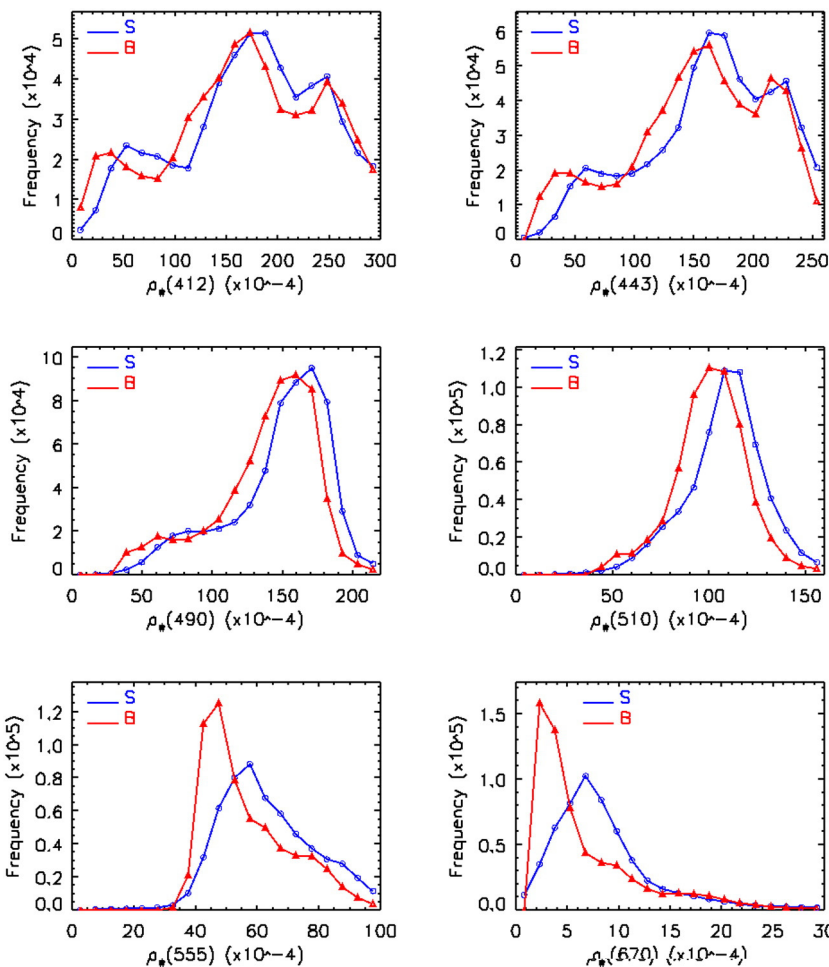


Fig. 19. Histograms of valid ρ_w estimates obtained with the Bayesian technique (B) and the SeaDAS algorithm (S). The Bayesian estimates are shifted toward lower values.

site). They are significantly larger, however, than the SeaDAS values at the BOUSSOLE site, i.e., 0.0045 at 412 nm, 0.0012 at 555 nm, and 0.0003 at 670 nm (Antoine et al., 2008), but in this case, like for the MOBY match-up data set, the sampling is limited to a single site.

One cannot conclude, however, based on the analysis of such limited match-up data, whether or not the Bayesian technique performs better, in terms of accuracy, than the SeaDAS algorithm. In the previous discussion of imagery (Section 8.1), evidence was provided that agreement between marine reflectance estimated by the Bayesian technique and the SeaDAS algorithm may occur in one part of an image, but not everywhere in the same image. The lack of comprehensive evaluation data emphasizes the importance of generalization in developing inversion schemes for global application, i.e., in our Bayesian approach, proper approximation of the forward operator.

9. Summary and conclusions

The inverse ocean-color problem, i.e., the retrieval of spectral marine reflectance from spectral TOA reflectance measurements, has been examined in a Bayesian context. This is motivated by the ill-posed nature of the problem (many possible antecedents), which stems first from the complexity of the forward operator that relates the variable to recover to the set of measurements and second from the noise in the measurements. By defining the general solution of the inverse problem as a probability distribution (the posterior distribution), the Bayesian paradigm allows one to quantify the likelihood of encountering specific values of the derived variable (marine reflectance) given the observed

variable (TOA reflectance or, in our modeling, the TOA reflectance corrected for molecular scattering effects).

The Bayesian approach makes it possible to incorporate known constraints of the marine reflectance (i.e., correlation between components) and to account for the varied sources of uncertainty (i.e., measurement noise, radiation transfer modeling errors). Importantly, it also permits the construction of reliable multi-dimensional confidence domains of the retrieved marine reflectance. These confidence domains are specific to each sample and can be constructed for any probability value. Specifically, the mean and covariance of the posterior distribution are computed. These quantities provide, for each pixel, an estimate of the marine reflectance and a measure of its uncertainty. The p -value, which quantifies how the TOA observation fits the forward model value, is also computed, allowing one to identify situations for which observation and model are incompatible. Thus the methodology offers the means to analyze and interpret ocean-color imagery in view of confidence limits and model adequacy, on a pixel-by-pixel basis. This is a definite advantage over standard atmospheric correction techniques, which rely essentially on evaluation against too few in situ measurements for accuracy assessments. Compared with other statistical techniques, e.g., Gross et al. (2007a,b) and Shroeder et al. (2007), which can be interpreted in a Bayesian context (since they approximate a conditional expectation implicitly defined from the distribution of simulated data), our approach is to first define formally the solution and then devise ways to approximate it.

The definitions of the Bayesian solution and of the inverse applications require a prior distribution on the oceanic and atmospheric parameters, and a noise distribution. The prior distribution on the marine reflectance has been defined by using the NOMAD and AERONET-OC data sets for

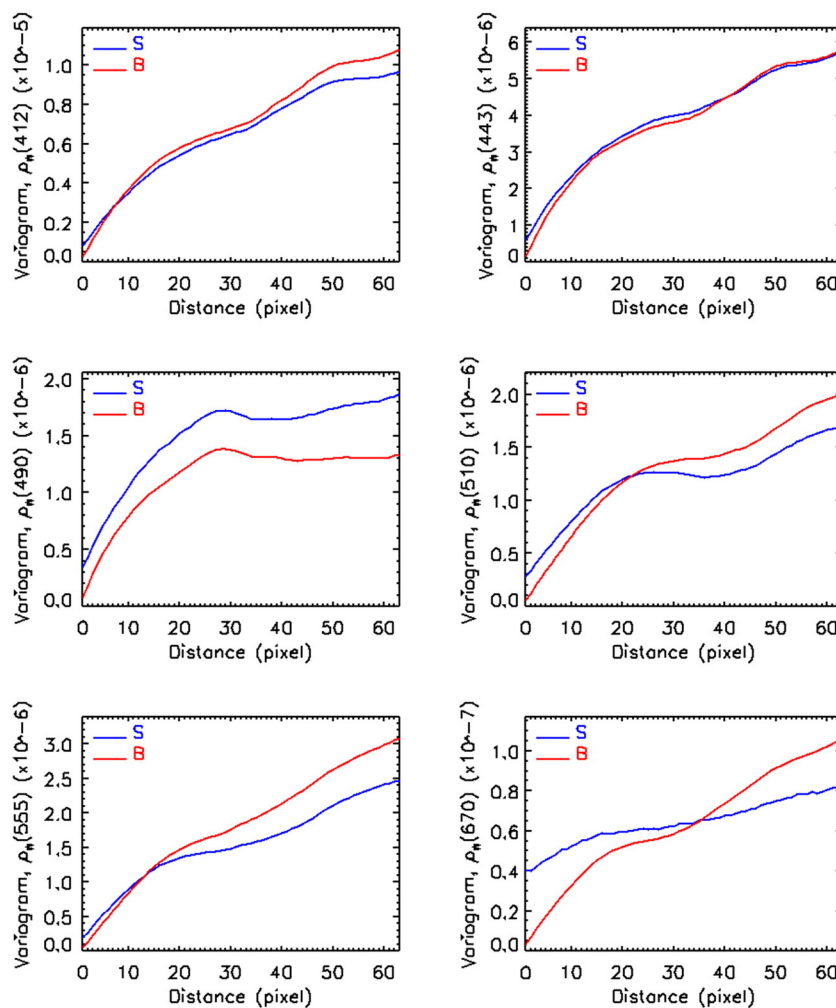


Fig. 20. Variograms of valid ρ_w estimates obtained with the Bayesian technique (B) and the SeaDAS algorithm (S). Computations are made using data in a 128×128 pixel area South of the Cape of Good Hope. The variograms obtained with the statistical method indicate less noisy retrievals.

marine reflectance. The data sets include situations of Case 1 and Case 2 waters, but not situations of very turbid waters containing sediments (e.g., estuarine waters). Our choice of using data instead of simulations for the marine reflectance was deliberate, dictated by the fact that models do not take fully into account the natural correlations between the intervening optical parameters (it is desirable not to introduce assumptions on the variable to retrieve). This makes it more difficult, however, to discretize properly the marine reflectance space (data not uniformly distributed, missing values). Since relatively little independent information (i.e., not resulting from inversion of satellite observations) is available about the global distribution of the atmospheric parameters and marine reflectance over the ocean, the prior distributions were considered uniform over the data sets, except for the aerosol optical thickness, which, based on a comprehensive in situ data set, was assumed to be distributed log-normally. For the noise, a normal distribution with zero mean was used, and its diagonal covariance matrix was determined by comparing a large and diverse ensemble of TOA reflectance extracted from actual satellite imagery with the output from the theoretical forward operator.

The theoretical inverse applications were approximated numerically based on extensive simulated data. The inverse applications models are all defined as piecewise constant, or piecewise linear, functions over the cells of a common partition of the space of TOA reflectances. The choice of models for the numerical approximations was based on several considerations, i.e., models fast in execution, convenience to approximate the conditional covariance (a second order quantity), and detection of abnormal cases (limitation of the forward model) by the p -value.

Partition-based models are suitable for these purposes; the partition is hierarchical, with hierarchy induced by a perfect binary tree, which drastically reduces the computational cost of determining cell membership. The parameters of the inverse models, defined for each point of the angular grid, need to be stored (like look-up tables in the standard scheme), but storage space is not an issue, even though the data set may be large. This makes the Bayesian methodology applicable operationally. It could be easily implemented (without special requirements) into the NASA OBPG processing system.

The inverse models were constructed for application to SeaWiFS imagery. Theoretical performance for this ocean-color sensor is good globally, i.e., on average over all the geophysical conditions and geometries considered, with negligible biases and standard deviation decreasing from 0.004 at 412 nm to 0.001 at 670 nm. Errors are smaller, however, for geometries that avoid Sun glint contamination and minimize air mass and aerosol influence. For example the standard deviation is reduced to 0.002–0.003 in the blue when the Sun and view zenith angles are 30° and the relative azimuth angle is 120°. Performance is degraded in the presence of Sun glint, but remains acceptable (<0.005 at 412 nm) in many situations. Errors increase with increasing optical thickness, reaching 0.009, 0.006, and 0.002 at 412, 555, and 670 nm, respectively, when the aerosol optical thickness at 550 nm is in the range 0.4–0.6. With respect to aerosol type, the larger standard deviations are obtained for atmospheres with continental or urban aerosols, and the smaller for atmospheres with maritime aerosols (the case over most of the open ocean). Biases are negative for mixtures dominated by the urban type,

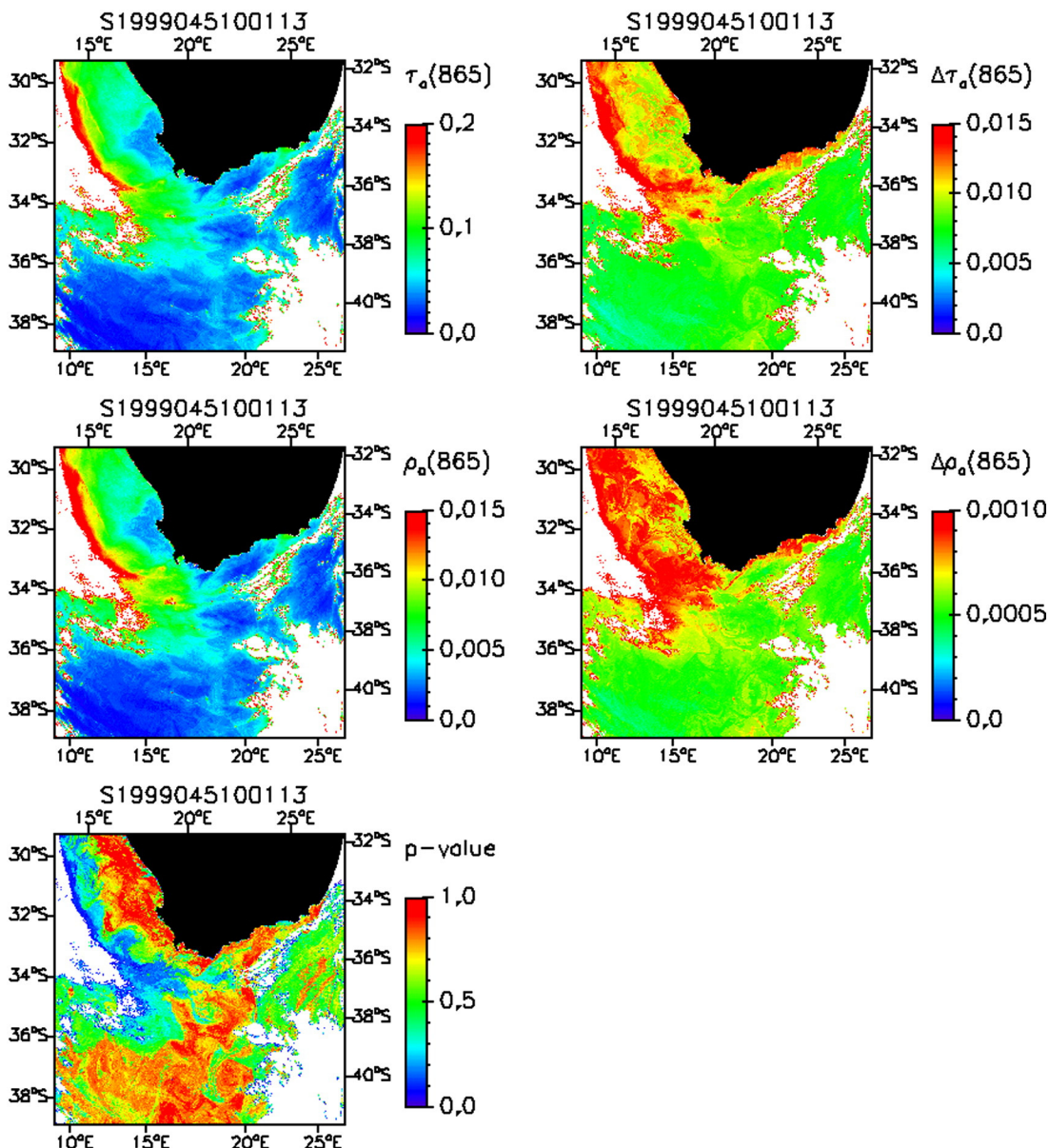


Fig. 21. Top panels: Estimated τ_a and τ_a standard deviation. Middle panels: Estimated ρ_a and ρ_a standard deviation. Bottom panel: *p*-Value.

and positive for mixtures dominated by continental aerosols, by a few 0.001 in magnitude in the blue and smaller at longer wavelengths, and they are small for mixtures dominated by the maritime type. Importantly, the estimated uncertainty (conditional covariance) is consistent with the inversion error, i.e., it provides a good measure of uncertainty.

Application to actual SeaWiFS imagery yielded marine reflectance fields with realistic features and patterns in view of the current knowledge of ocean circulation and biogeochemistry. The retrieved fields exhibited good continuity near clouds, and they did not exhibit significant correlation with the corresponding fields of atmospheric variables. Uncertainty generally remained within ± 0.003 in the blue, except near clouds and where the aerosol optical thickness was large. The *p*-value was mostly above 0.05, but often above 0.5, indicating good compatibility between forward model and observation. Compared with the marine reflectance fields obtained from the SeaDAS algorithm, the Bayesian fields do not exhibit systematic biases, but they are less noisy, and they have different de-correlation scales. Note that standard, yet very conservative flags were applied to the selected SeaWiFS imagery to eliminate observations with clouds, Sun glint, and too high aerosol reflectance, i.e., the Bayesian methodology was not tested for such

situations. In view of the theoretical performance, however, reasonable estimates are expected in the presence of Sun glint, absorbing aerosols, and fairly high aerosol optical thickness, and possibly in the presence of thin clouds since they may be interpreted as aerosols. Those situations, as well as a variety of oceanic cases, will be examined in a future study.

Compared with marine reflectance measurements, the Bayesian estimates exhibit RMS differences of 0.005, 0.0004, and 0.00005 at 412, 555, and 670 nm (MOBY data set) and 0.006, 0.003, and 0.001, respectively (NOMAD data set). These values are comparable with those expected from the theoretical analysis of performance and the values obtained with the SeaDAS algorithm during various evaluation activities. The Bayesian estimates, however, are biased high at the MOBY site, which was plausibly explained by the aerosols prevailing at the site and the algorithm performance for those aerosols. One cannot conclude, from examining such a limited match-up data set, whether the Bayesian methodology is more accurate.

The performance of the Bayesian methodology depends critically on the characteristics of the prior distributions (i.e., how they are specified). Due to lack of information, the distributions were taken as uniform over the space of the various variables, except for the aerosol optical

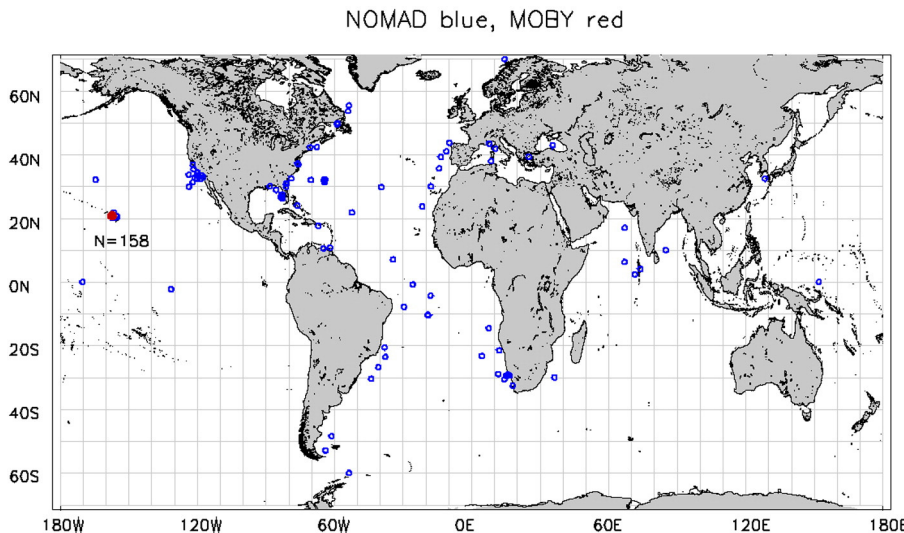


Fig. 22. Geographic location of the NOMAD and MOBY match-up data sets.

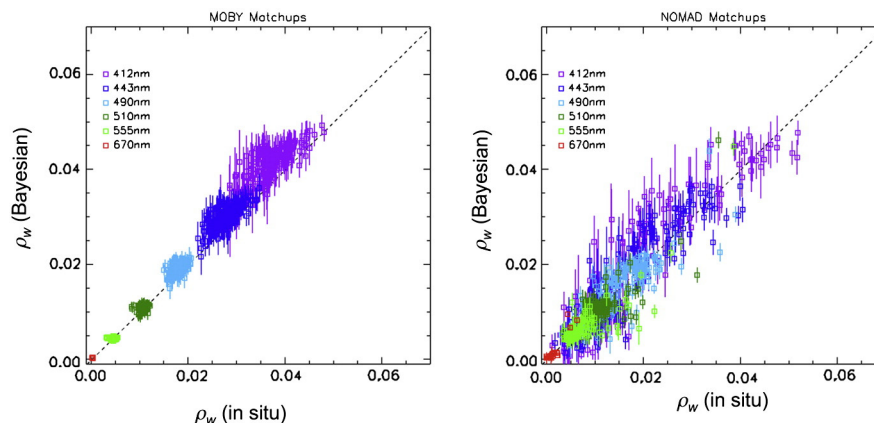


Fig. 23. Estimated versus measured marine reflectance for MOBY and NOMAD match-up data sets.

thickness. But one could have taken into account that Case 2 waters and continental and pollution aerosols are more likely to be encountered in coastal regions. Such information may help to constrain the Bayesian solution and, therefore, improve retrieval accuracy. It may originate from various (independent) sources, in particular simulations by global numerical models of the atmosphere and ocean. These models predict, regionally, the temporal variability of key variables in the forward modeling, for example the likelihood of encountering a certain aerosol type and vertical profile or a certain chlorophyll concentration (from which one may deduce some information about marine reflectance variability). Due to the ill-posed nature of the inverse problem, this “regionalization” aspect is key to improving performance in situations difficult to deal with, such as absorbing aerosols and optically complex waters. Since these situations occur in biologically productive regions, in general the coastal zone, the expected gain in accuracy for

biogeochemistry studies would be significant. “Regionalization” of the Bayesian methodology, as well as extending the methodology to other satellite sensors, and further evaluation, will be addressed in future work.

Acknowledgments

Funding for this work has been provided by NASA under grants NNX11AR07G and NNX11AI36G. The technical support of Mr. John McPherson from the Scripps Institution of Oceanography, University of California at San Diego, is gratefully acknowledged. The authors also thank the NASA OBPG, the NOAA MOBY Project, and the NASA AERONET-OC Project for making available the satellite and in-situ data sets used in the study, and three anonymous reviewers for scrutinizing in detail the manuscript and providing valuable comments and suggestions.

Table 8

Comparison statistics of marine reflectance estimated by the Bayesian technique and measured in situ (MOBY match-up data set).

λ (nm)	Average ρ_w	r^2	Bias	RMS difference	No. points
412	0.03687	0.599	0.00407	0.00491	132
443	0.02778	0.485	0.00236	0.00306	144
490	0.01801	0.201	0.00112	0.00159	144
510	0.01071	0.034	0.00010	0.00072	113
555	0.00464	0.001	-0.00018	0.00040	129
670	0.00034	0.003	-0.00001	0.00005	28
All	0.01639	0.987	0.00124	0.00247	690

Table 9

Same as Table 8, but NOMAD data set.

λ (nm)	Average ρ_w	r^2	Bias	RMS difference	No. points
412	0.02049	0.838	0.00164	0.00593	158
443	0.01799	0.806	0.00088	0.00449	158
490	0.01545	0.670	-0.00025	0.00346	158
510	0.01155	0.587	-0.00049	0.00301	158
55	0.00712	0.722	-0.00074	0.00258	158
670	0.00133	0.820	-0.00008	0.00121	158
All	0.01418	0.852	0.00023	0.00403	948

Appendix A. Missing data inference

To illustrate the methodology, consider the problem of estimating the (missing) value of ρ^{670} based on measurements of $\rho^{412}, \dots, \rho^{555}$, where ρ^λ denotes the marine reflectance in spectral band λ . Suppose that at our disposal is a random sample of size n of complete observations $(\rho_i^{412}, \dots, \rho_i^{670})$, for $i = 1, \dots, n$. The procedure consists in estimating the conditional expectation $\mathbb{E}[\rho^{670} | \rho^{412}, \dots, \rho^{555}]$ from the n complete data. The rationale behind this estimate is that the conditional expectation is the best approximation of ρ^{670} that can be constructed based solely on the information conveyed by $\rho^{412}, \dots, \rho^{555}$, where optimality is understood in the sense of the average quadratic loss criterion.

Estimating the conditional expectation from the data is a standard nonparametric regression estimation problem. Numerous techniques exist for this purpose (see, e.g., Györfi et al., 2002) and in this work, we considered a k -nearest neighbor regression estimate. The regression estimate is constructed using the n complete data (here $n = 729$) and is next applied to each spectrum containing one missing value. The algorithm is detailed in Table A.1 for the estimation of the missing value of ρ^{670} from $\rho^{412}, \dots, \rho^{555}$. The procedure is repeated for each of the 6 spectral bands where one value is missing. This results in a complete data set of 2651 Case I marine reflectance spectra.

Table A.1

k -Nearest neighbor (k -NN) algorithm for the estimation of the missing values in the marine reflectance spectra. Illustration for the estimation of the marine reflectance at 670 nm based on the measurements at smaller wavelengths.

<i>k</i> -NN algorithm for missing value estimation: estimation of ρ^{670} from $\rho^{412}, \dots, \rho^{555}$	
1. Input:	$\rho := (\rho^{412}, \dots, \rho^{555})$ and the complete data $(\rho_i^{412}, \dots, \rho_i^{670})$ for $i = 1, \dots, n$.
2. For each complete data $(\rho_i^{412}, \dots, \rho_i^{670})$, compute its distance d_i to ρ according to:	
	$d_i = \left[(\rho_i^{412} - \rho^{412})^2 + \dots + (\rho_i^{555} - \rho^{555})^2 \right]^{\frac{1}{2}}.$
3. Sort the distances in increasing order: $d_{(1)} \leq \dots \leq d_{(n)}$.	
4. Select the k observations $\rho_{(1)}^{670}, \dots, \rho_{(k)}^{670}$ corresponding to the k smallest distances of step 3.	
5. Output:	the estimate $\hat{\rho}^{670}$ as the average of the observations selected at step 4, i.e.,
	$\hat{\rho}^{670} = \frac{1}{k} \sum_{j=1}^k \rho_{(j)}^{670}.$

Appendix B. Tree-based partition rules

To guarantee convergence of a density or regression model, for instance, based on a partition, typically the number of cells must go to infinity while the cells must shrink at an appropriate rate; see, e.g., Lugosi and Nobel (1999) and Nobel (1996). Several techniques have been developed to try to infer an optimal set of splitting rules (or even an optimal tree) from the data, especially to prevent over-fitting; see Breiman et al. (1984) and the literature on random forests (Breiman, 2001). As exposed above, to keep the execution of the models quick, the partition is induced by a perfect binary tree. To determine suitable splitting rules, we first simulate a number n of TOA reflectances y_1, \dots, y_n according to model (9). The splitting rules are then defined recursively as follows. For each node to split, we select the axis j such that the j th component of the simulated data has maximal variance. Next, the split threshold δ is set as the median of the component of the data corresponding to this axis. The procedure is then repeated successively, starting from the root node to the leaves of the tree, until all the splitting rules are computed. The whole algorithm is summarized in Table B.1. Note that since the split threshold is taken as the median along a certain axis, at each node, a data point has an equal probability of being moved to the left child as to the right child. Therefore all the cells of the partition have equal probability content, i.e., the probability that y falls in a given cell of the partition is constant and equal to $1/2^K$ for a tree of depth K , since it contains 2^K leaves.

In the present work, we have taken $K = 17$ which yields a partition with $2^K = 131,072$ cells. The number n of simulated points used to

determine the splitting rules is 140 millions. As a final comment, the algorithm is not run on the canonical basis of \mathbb{R}^d , as described herein for simplicity, but on the basis of the eigenvectors of the covariance matrix of y .

Table B.1

Construction algorithm of the tree structured partition associated with a perfect binary tree of depth K .

Construction algorithm of the tree-structured partition	
1. Input:	Data y_1, \dots, y_n and depth K .
2.	Associate the n data to the root node.
3.	Compute the variances on each axis.
4.	Select the axis j corresponding to the maximal variance.
5.	Sort the j th component of the data in ascending order: $y_{(1)}^j \leq y_{(2)}^j \leq \dots \leq y_{(n)}^j$, and set the split value as the median of the (univariate) ordered sample, e.g., as $\delta = \frac{1}{2} (y_{(n/2)}^j + y_{(n/2+1)}^j)$ if n is even.
6.	Move the data whose j th component is lower than δ to the left child, and otherwise to the right child.
7.	Repeat the above procedure on the left and right children until all the nodes up to depth K are constructed.
8. Output:	A perfect binary tree with depth K and the splitting rules of the form (j, δ) for each internal node.

References

- Antoine, D., d'Ortenzio, F., Hooker, S.B., Béchu, G., Gentilli, B., Tailliez, D., et al. (2008). Assessment of uncertainty in the ocean reflectance determined by three satellite ocean color sensors (Meris, SeaWiFS, and MODIS-A) at an offshore site in the Mediterranean Sea (BOUSSOLE project). *Journal of Geophysical Research*. <http://dx.doi.org/10.1029/2007JC004472>.
- Antoine, D., & Morel, A. (1999). A multiple scattering algorithm for atmospheric correction of remotely sensed ocean colour (MERIS instrument): Principle and implementation for atmospheres carrying various aerosols including absorbing ones. *International Journal of Remote Sensing*, 20, 1875–1916.
- Bailey, S., Franz, B., & Werdell, P. (2010). Estimation of near-infrared water-leaving reflectance for satellite ocean color data processing. *Optics Express*, 18, 7521–7527.
- Bélanger, S., Ehn, J., & Babin, M. (2007). Impact of sea ice on the retrieval of water-leaving reflectance, chlorophyll a concentration and inherent optical properties from satellite ocean color data. *Remote Sensing of Environment*, 111, 51–68.
- Biau, G., Cadre, B., & Pelletier, B. (2008). Exact rates in density support estimation. *Journal of Multivariate Analysis*, 99, 2185–2207.
- Bissantz, N., Hohage, T., & Munk, A. (2004). Consistency and rates of convergence of nonlinear Tikhonov regularization with random noise. *Inverse Problems*, 20, 1773–1789.
- Bo-Cai, G., Montes, M. J., Ahmad, Z., & Davis, C. O. (2000). Atmospheric correction algorithm for hyperspectral remote sensing of ocean color from space. *Applied Optics*, 39, 887–896.
- Brajard, J., Jamet, C., Moulin, C., & Thiria, S. (2006). Use of a neuro-variational inversion for retrieving oceanic and atmospheric constituents from satellite ocean color sensor: Application to absorbing aerosols. *Neural Networks*, 19, 178–185.
- Breiman, L. (2001). Random forests. *Machine Learning*, 45, 5–32.
- Breiman, L., Friedman, J., Olshen, R., & Stone, C. (1984). *Classification and regression trees*. Chapman and Hall.
- Buriez, J., & Fouquart, Y. (1980). Generalization of the Curtis–Godson approximation to inhomogeneous scattering atmospheres. *Journal of Quantitative Spectroscopy and Radiative Transfer*, 24, 407–419.
- Chomko, R., & Gordon, H. (1988). Atmospheric correction of ocean color imagery: Use of the Jungle power-law aerosol size distribution with variable refractive index to handle aerosol absorption. *Applied Optics*, 37, 5560–5572.
- Clark, D.K., Yarbrough, M.A., Feinholz, M., Flora, S., Broenkow, W., Kim, Y.S., et al. (2003). Moby, a radiometric buoy for performance monitoring and vicarious calibration of satellite ocean color sensors: Measurement and data analysis protocols. In J.L. Mueller, G.S. Fargion, & C.R. McClain (Eds.), *NASA Tech. Memo.*, Vol. VI, Greenbelt, MD: NASA GSFC (2003 D 211621/Rev4, 139 pp.).
- Cox, C., & Munk, W. (1954). Measurement of the roughness of the sea surface from photographs of the sun's glitter. *Journal of the Optical Society of America*, 44, 838–850.
- Deschamps, P., Herman, M., & Tanré, D. (1983). Modélisation du rayonnement réfléchi par atmosphère et la terre, entre 0.35 et 4 μm. *ESA Contract Report No. 4393/8C/F-DD(SC)* (156 pp.).
- Deuzé, J., Herman, M., & Santer, R. (1989). Fourier series expansion of the transfer equation in the atmosphere–ocean system. *Journal of Quantitative Spectroscopy and Radiative Transfer*, 41, 483–494.
- Doney, S.C., Glover, D.M., McCue, S.J., & Fuentes, M. (2003). Mesoscale variability of sea-viewing wide field-of-view sensor (SeaWiFS) satellite ocean color: Global patterns and spatial scales. *Journal of Geophysical Research*, 108. <http://dx.doi.org/10.1029/2001JC000843>.
- Engl, H., Hanke, K., & Neubauer, A. (1996). *Regularization of inverse problems*. Kluwer.
- Frouin, R., Deschamps, P.-Y., Gross-Colzy, L., Murakami, H., & Nakajima, T. (2006). Retrieval of chlorophyll-a concentration via linear combination of global imager data. *Journal of Oceanography*, 62, 331–337.

- Frouin, R., & Pelletier, B. (2007). Fields of non-linear regression models for atmospheric correction of satellite ocean-color imagery. *Remote Sensing of Environment*, 111, 450–465.
- Frouin, R., Schwindling, M., & Deschamps, P.-Y. (1996). Spectral reflectance of sea foam in the visible and near infrared: In-situ measurements and remote sensing implications. *Journal of Geophysical Research*, 101, 14361–14371.
- Garver, S., & Siegel, D. (1997). Inherent optical property inversion of ocean color spectra and its biogeochemical interpretation. *Journal of Geophysical Research*, 102, 18607–18625.
- Goody, R. (1964). *Atmospheric radiation, 1. Theoretical basis*. Oxford University Press.
- Gordon, H.R. (1997). Atmospheric correction of ocean color imagery in the earth observing system era. *Journal of Geophysical Research*, 102, 17081–17106.
- Gordon, H., Brown, O., Evans, R., Brown, J., Smith, R., & Baker, K. (1988). A semi-analytical radiance model of ocean color. *Journal of Geophysical Research*, 93, 10909–10924.
- Gordon, H., Du, T., & Zhang, T. (1997). Remote sensing of ocean color and aerosol properties: Resolving the issue of aerosol absorption. *Applied Optics*, 36, 8670–8684.
- Gross, L., Colzy, S., Frouin, R., & Henry, P. (2007a). A general ocean color atmospheric correction scheme based on principal components analysis part I: Performance on case 1 and case 2 waters. In R. Frouin, & Z. Lee (Eds.), *Proc. SPIE*, Vol. 6680, . <http://dx.doi.org/10.1117/12.738508>.
- Gross, L., Colzy, S., Frouin, R., & Henry, P. (2007b). A general ocean color atmospheric correction scheme based on principal components analysis part II: Level 4 merging capabilities. In R. Frouin, & Z. Lee (Eds.), *Proc. SPIE*, Vol. 6680, . <http://dx.doi.org/10.1117/12.738514>.
- Gyorfi, L., Kohler, M., Krzyzak, A., & Walk, H. (2002). *A distribution-free theory of nonparametric regression*. New-York: Springer.
- Hu, C., Carder, K., & Muller-Karger, F. (2000). Atmospheric correction of SeaWiFS imagery over turbid coastal waters: A practical method. *Remote Sensing of Environment*, 74, 195–206.
- Jamet, C., Thiria, S., Moulin, C., & Crépon, M. (2005). Use of a neurovariational inversion for retrieving oceanic and atmospheric constituents from ocean color imagery: A feasibility study. *Journal of Atmospheric and Oceanic Technology*, 22, 460–475.
- Kaipio, J., & Somersalo, E. (2004). *Statistical and computational inverse problems*. Berlin: Springer.
- Knobelspiesse, K.D., Pietras, C., Fargion, G., Wang, M., Frouin, R., Miller, M., et al. (2004). Maritime aerosol optical thickness measured by handheld sunphotometers. *Remote Sensing of Environment*, 93, 87–106.
- Koepke, P. (1984). Effective reflectance of oceanic whitecaps. *Applied Optics*, 23, 1816–1824.
- Kuchinke, C., Gordon, H., Harding, L., & Voss, K. (2009). Spectral optimization for constituent retrieval in case 2 waters I: Implementation and performance. *Remote Sensing of Environment*, 113, 571–587.
- Land, P., & Haigh, J. (1996). Atmospheric correction over case 2 waters using an iterative fitting algorithm. *Applied Optics*, 35, 5443–5451.
- Lavender, S., Pinkerton, M., Moore, G., Aiken, J., & Blondeau-Patissier, D. (2005). Modification of the atmospheric correction of SeaWiFS ocean colour images over turbid waters. *Continental Shelf Research*, 25, 539–555.
- Lee, Z. (2006). Remote sensing of inherent optical properties: Fundamentals, tests of algorithms and applications. *Technical report*, 5, IOCCG.
- Lenoble, J., Herman, M., Deuzé, J.-L., Lafrance, B., & Tanré, D. (2007). A successive orders of scattering code for solving the vector equation of transfer in the earth's atmosphere with aerosols. *Journal of Quantitative Spectroscopy and Radiation Transfer*, 107, 479–507.
- Lugosi, G., & Nobel, A. (1999). Consistency of data-driven histogram methods for density estimation and classification. *Annals of Statistics*, 27, 1830–1864.
- Malkmus, W. (1967). Random Lorentz band model with exponential-tailed $s - 1$ line intensity distribution function. *Journal of the Optical Society of America*, 53, 323–329.
- Morel, A., & Belanger, S. (2006). Improved detection of turbid waters from ocean color sensors information. *Remote Sensing of Environment*, 102, 237–249.
- Morel, A., & Gentili, B. (1993). Diffuse reflectance of oceanic waters, 2. Bidirectional aspects. *Applied Optics*, 32, 6864–6879.
- Morel, A., & Maritorena, S. (2002). Bio-optical properties of oceanic waters: A reappraisal. *Journal of Geophysical Research*, 106, 7163–7180.
- Morel, A., Voss, K., & Gentili, B. (1995). Bidirectional reflectance of oceanic waters: A comparison of modeled and measured upward radiance fields. *Journal of Geophysical Research*, 100, 13143–13150.
- Nicolas, J.-M., Deschamps, P.-Y., & Frouin, R. (2001). Spectral reflectance of oceanic whitecaps in the visible and near infrared: Aircraft measurements over open ocean. *Geophysical Research Letters*, 28, 4445–4448.
- Nobel, A. (1996). Histogram regression estimation using data dependent partitions. *Annals of Statistics*, 24, 1084–1105.
- O'Reilly, J., Maritorena, S., Mitchell, B., Siegel, D., Carder, K., Garver, S., et al. (1998). Ocean colour chlorophyll algorithms for SeaWiFS. *Journal of Geophysical Research*, 103, 24937–24953.
- Oo, M., Vargas, M., Gilerson, A., Gross, B., Moshary, F., & Ahmed, S. (2008). Improving atmospheric correction for highly productive coastal waters using the short wave infrared retrieval algorithm with water-leaving reflectance constraints at 412 nm. *Applied Optics*, 47, 3846–3859.
- Park, Y., & Ruddick, K. (2005). Model of remote sensing reflectance including bidirectional effects for case 1 and case 2 waters. *Applied Optics*, 44, 1236–1249.
- Pelletier, B., & Frouin, R. (2004). Fields of nonlinear regression models for inversion of satellite data. *Geophysical Research Letters*, 31, L16304. <http://dx.doi.org/10.1029/2004GL019840>.
- Pelletier, B., & Frouin, R. (2005). Remote sensing of phytoplankton chlorophyll-a concentration by use of ridge function fields. *Applied Optics*, 45(4), 784–798.
- Polonik, W. (1995). Measuring mass concentrations and estimating density contour clusters – An excess mass approach. *Annals of Statistics*, 23, 855–881.
- Polonik, W. (1997). Minimum volume sets and generalized quantile processes. *Stochastic Processes and their Applications*, 69, 1–24.
- Ruddick, K., Ovidio, F., & Rijkeboer, M. (2000). Atmospheric correction of SeaWiFS imagery for turbid and inland waters. *Applied Optics*, 39, 897–912.
- Santer, R., & Schmechtig, C. (2000). Adjacency effects on water surfaces: Primary scattering approximation and sensitivity study. *Applied Optics*, 39, 361–375.
- Schoeder, T., Behnert, I., Schaale, M., Fischer, J., & Doerffer, R. (2007). Atmospheric correction algorithm for MERIS above case-2 waters. *International Journal of Remote Sensing*, 28, 1469–1486.
- Siegel, D., Wang, M., Maritorena, S., & Robinson, W. (2000). Atmospheric correction of satellite ocean color imagery: The black pixel assumption. *Applied Optics*, 39, 3582–3591.
- Smirnov, A., Holben, B.N., Dubovik, O., Frouin, R., & Slutsker, I. (2003). Maritime component in aerosol optical models derived from AERONET (Aerosol Robotic Network) data. *Journal of Geophysical Research*, 108. <http://dx.doi.org/10.1029/2002JD002701>.
- Stamnes, K., Li, W., Yan, B., Elde, H., Barnard, A., Pegau, S., et al. (2007). Accurate and self-consistent ocean color algorithm: simultaneous retrieval of aerosol optical properties and chlorophyll concentrations. *Applied Optics*, 42, 939–951.
- Steinmetz, F., Deschamps, P., & Ramon, D. (2011). Atmospheric correction on the presence of sun glint: Application to meris. *Optics Express*, 19, 9783–9800.
- Stumpf, R., Arnone, R., Gould, R., Martinolich, P., & Ransibrahmanakul, V. (2003). A partially coupled ocean-atmosphere model for retrieval of water-leaving radiance from seaWiFS in coastal water. *Algorithm updates for the fourth SeaWiFS data reprocessing*. *SeaWiFS Post-Launch Technical Series*, Vol. 22, .
- Tanré, D., Herman, M., Deschamps, P.-Y., & De Leffe, A. (1979). Atmospheric modeling for space measurements of ground reflectances, including bidirectional properties. *Applied Optics*, 18, 3587–3594.
- Tarantola, A. (2005). *Inverse problem theory*. SIAM.
- Wang, M. (2010). Atmospheric correction for remotely-sensed ocean-colour products. *Technical report*, 10, IOCCG.
- Wang, M., Son, S., & Shi, W. (2009). Evaluation of MODIS SWIR and NIR-SWIR atmospheric correction algorithm using SeaBASS data. *Remote Sensing of Environment*, 113, 635–644.
- Wang, M., Tang, T., & Shi, W. (2007). MODIS-derived ocean color products along the China east coastal region. *Geophysical Research Letters*, L06611. <http://dx.doi.org/10.1029/2006GL02859>.
- Werdell, P., & Bailey, S. (2005). An improved in-situ bio-optical data set for ocean color algorithm development and satellite data product validation. *Remote Sensing of Environment*, 98, 122–140.
- WMO (1983). *Radiation commission of IAMAP meeting of experts on aerosol and their climatic effects*. Williamsburg VA: WCP55, 28–30.
- Zibordi, G., Holben, B., Mélin, F., DALimonte, D., Berthon, J., Slutsker, I., et al. (2010). AERONET-OC: An overview. *Canadian Journal of Remote Sensing*. <http://dx.doi.org/10.5589/m10-073>.
- Zibordi, G., Holben, B., Slutsker, I., Giles, D., DALimonte, D., Mélin, F., et al. (2009). AERONET-OC: A network for the validation of ocean color primary products. *Journal of Atmospheric and Oceanic Technology*, 26, 1634–1651.